PNNL-15581

Pacific Northwest
National Laboratory
Operated by Battelle for the
U.S. Department of Energy

FY 2005 Infrared Photonics Final Report

N. C. Anheier,Jr.
P. J. Allen
N. Hô
K. Krishnaswami
B. R. Johnson
K. Sundaram
B. J. Riley
J. E. Martinez
A. Qiao
J. F. Schultz

December 2005

Prepared for the U.S. Department of Energy
under Contract DE-AC05-76RL01830

DISCLAIMER

PACIFIC NORTHWEST NATIONAL LABORATORY
operated by
BATTELLE
for the
UNITED STATES DEPARTMENT OF ENERGY
under Contract DE-AC05-76RL01830

Printed in the United States of America

Available to DOE and DOE contractors from the
Office of Scientific and Technical Information,
P.O. Box 62, Oak Ridge, TN 37831-0062;
ph: (865) 576-8401
fax: (865) 576-5728
email: reports@adonis.osti.gov

Available to the public from the National Technical Information Service,
U.S. Department of Commerce, 5285 Port Royal Rd., Springfield, VA 22161
ph: (800) 553-6847
fax: (703) 605-6900
email: orders@ntis.fedworld.gov
online ordering: http://www.ntis.gov/ordering.htm

This document was printed on recycled paper.
(9/2003)

PNNL-15581

FY 2005 Infrared Photonics Final Report

N. C. Anheier
P. J. Allen
N. Hô
K. Krishnaswami
B. R. Johnson
S. K. Sundaram
B. J. Riley
J. E. Martinez
A. Qiao
J. F. Schultz

December 2005

Prepared for
the U.S. Department of Energy
under Contract DE-AC05-76RL01830

Pacific Northwest National Laboratory
Richland, Washington 99352

Summary

Research done by the Infrared Photonics team at Pacific Northwest National Laboratory (PNNL) is focused on developing miniaturized integrated optics for mid-wave infrared (MWIR) and long-wave infrared (LWIR) sensing applications by exploiting the unique optical and material properties of chalcogenide glass. PNNL has developed thin-film deposition capabilities, direct laser writing techniques, infrared photonic device demonstration, holographic optical element design and fabrication, photonic device modeling, and advanced optical metrology—all specific to chalcogenide glass. Chalcogenide infrared photonics provides a pathway to quantum cascade laser (QCL) transmitter miniaturization. QCLs provide a viable infrared laser source for a new class of laser transmitters capable of meeting the performance requirements for a variety of national security sensing applications. The high output power, small size, and superb stability and modulation characteristics of QCLs make them amenable for integration as transmitters into ultra-sensitive, ultra-selective point sampling and remote short-range chemical sensors that are particularly useful for nuclear nonproliferation missions.

During FY 2005, PNNL's Infrared Photonics research team made measurable progress exploiting the extraordinary optical and material properties of chalcogenide glass to develop miniaturized integrated optics for mid-wave infrared (MWIR) and long-wave infrared (LWIR) sensing applications. We investigated sulfur purification methods that will eventually lead to routine production of optical quality chalcogenide glass. We also discovered a glass degradation phenomenon and our investigation uncovered the underlying surface chemistry mechanism and developed mitigation actions. Key research was performed to understand and control the photomodification properties. This research was then used to demonstrate several essential infrared photonic devices, including LWIR single-mode waveguide devices and waveguide couplers. Optical metrology tools were also developed to characterize optical waveguide structures and LWIR optical components.

The Infrared Photonics research is positioned to develop chalcogenide-based photonic components such as waveguides, beam splitters, multiplexers, couplers, beam shapers, Bragg reflectors, long-period gratings, hybrid lenses, and polarizers. The integration of these guided-wave photonic components on a single substrate along with the QC lasers, all in a single package, provides a compact solution that meets the goals of infrared sensing missions.

Contents

Figures

Tables

1.0 Introduction

Chalcogenide glasses are attractive materials for fabricating mid-wave infrared (MWIR) and long-wave infrared (LWIR) photonic components because they combine relatively low transmission losses with the unique photomodification phenomenon. Amorphous semiconductors such as chalcogenide glasses exhibit a number of effects that are unique to the amorphous phase. They can undergo various transformations between different phases while being illuminated by a given photon energy. One of these transformations is photodarkening, which corresponds to a photo-induced red shift of the absorption spectrum. For photon energy below the band-gap energy, this shift leads to an increase of the refractive index. It is thus possible to use this effect in a controlled manner to create waveguides, and any structure can be patterned in the glass by either moving a focused beam in or on the glass or exposing the glass through an amplitude or phase mask. Chalcogenide glasses exposed with band-gap energy light can undergo a large refractive index change in the infrared spectrum, and values approaching 0.1 have been reported. With proper characterization of the photodarkening effect in thin films, which can differ from that in bulk samples, laser writing of waveguides, couplers, cavities, and other complex optical devices for the infrared sensing application can therefore be achieved in chalcogenide glasses.

By exploiting the unique and exciting properties of the chalcogenide glass family, Pacific Northwest National Laboratory (PNNL) is developing the photonic optical components needed to miniaturize infrared sensing systems. This research will create a pathway toward efficient, compact, field-deployable systems that will meet the sensing needs of national security missions.

In this report we provide a summary of the FY 2005 research progress for the Infrared Photonics project. Background information on PNNL's chalcogenide infrared photonics research can be found in our prior report (Anheier et. al. 2004). In Section 2, we summarize the sulfur purification investigation that will eventually lead to routine production of optical quality chalcogenide glass. In Section 3, we discuss a glass degradation phenomenon and our investigation to uncovered the underlying surface chemistry mechanism. In Section 4, we provide an update on the improvements in the chalcogenide thin film deposition system and in Section 5, we report on the effects of annealing on the photodarkening process. In Section 6, we discuss our development efforts to demonstrate several essential infrared photonic devices, including LWIR single-mode waveguide devices and waveguide couplers. Section 7 describes the development of powerful optical metrology tools needed to characterize optical waveguide structures and LWIR optical components.

2.0 Chalcogenide Glass Research and Development

During FY 2005, PNNL's Non-Oxide Materials Synthesis Laboratory continued delivering leading research and development in chalcogenide glass research. Chalcogenide glass production at PNNL is unique among the national laboratory facilities. Worldwide, only a handful of facilities are capable of producing chalcogenide glass needed for infrared optical applications. In addition, the commercial availability is limited to just a few glass formulations. In-house glass synthesis expertise is crucial to the success of the infrared photonics development goals. Consequently, significant progress was accomplished during the fiscal year to develop synthesize high-purity, low-loss infrared (IR) chalcogenide materials. The synthesis research was focused on improving the optical quality of the materials produced.

2.1 Sulfur Purification and Distillation

Commercially "pure" sulfur is contaminated with aliphatic (long chain) hydrocarbons, which upon heating, these contaminates polymerize to form a black, insoluble, carbon-sulfur polymer termed "carsul" (Susman et al. 1992). This has been consistent with our experience, as we have observed black deposits that form in sulfide based chalcogenide glasses, as well as various absorption peaks in FT-IR spectra in As-S glasses that are not found in As-Se glasses. Increased processing times and extended melting times of As_2S_3 glass has resulted in increased formation of these black deposits, which is predictable based on published data (Susman et al. 1992). These deposits have also been observed in commercially obtained As_2S_3, further highlighting the significance of this problem. Our efforts have been focused on adapting sulfur purification based on dynamic pyrolysis followed by distillation to produce high quality glass. Adaptation of this process has involved several design modifications as well as the development, fabrication, and testing of several engineering safety control systems (to prevent over-pressurization and over-heating) and approval of standard operating procedures for these experiments.

Complete purification via the dynamic pyrolysis method is expected to take up to 120 h, per the literature data. Our intent was to demonstrate an initial proof-of-concept and verify that the purification process was effective, possibly in shorter time. We have performed approximately 27 h of dynamic pyrolysis, distilled the sulfur, fabricated arsenic trisulfide glass from the purified sulfur, and analyzed it with FT-IR. The results demonstrate that there is indeed a carbon-based contaminant in commercially pure sulfur that is effectively polymerized by the dynamic pyrolysis method, and that distillation is capable of separating the purified product from the contaminant. Consequently, we are confident we will be able to produce improved, high-purity, chalcogenide glass materials using this purified sulfur. Additional work is planned in the early FY06 to refine the processing conditions, and determine the purification end-point for our specific process, subject to the availability of funding.

After performing the initial dynamic pyrolysis experiments last month, effort was focused on developing a means to separate pure sulfur from that contaminated with carsul. Distillation was the method chosen to do this, based again on Susman's work. The team was able to complete several distillation runs utilizing four independent heat sources to keep the pyrolysis kettle, pyrolysis lid, receiver arm, receiver lid, and receiver flask at a high enough temperature to prevent sulfur vapor condensation in the pathway from the pyrolysis flask to the receiver flask. The four independent heat sources included were the mantel heater, the silicone tape heater, the silicone tube heater, and the refractory wool tape heater. Each heater required the use of a separate temperature controller. See Figure 2.1A for a picture of the distillation setup.

Approximately 22.9 g of sulfur was distilled and collected in the receiving flask. As seen in Figure 2.1 B, the slug of pyrolyzed, residual contaminated sulfur left behind after distillation remained in the pyrolysis flask in a cohesive, dark, grayish mass, which was easily removable from the flask. The distilled sulfur is shown in Figure 2.2.

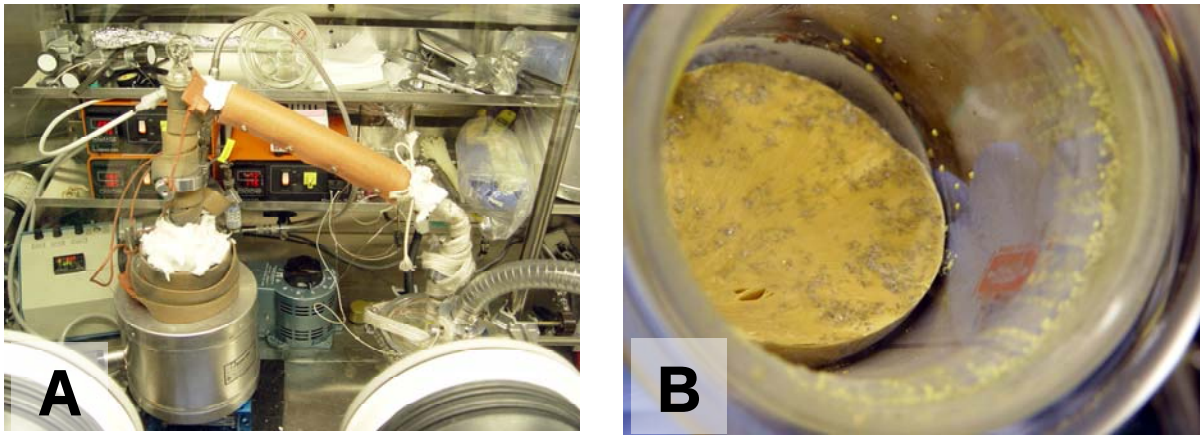

Figure 2.1. Left: Distillation apparatus; Right: The easy removal of the pyrolyzed, yet undistilled, sulfur slug.

We have pursued analytical techniques for quantifying the impurity levels in our sulfur samples. Susman's work utilized quantitative FT-IR transmission analysis of "neat" (pure sulfur) pellets. We have attempted FT-IR analysis on both neat pellets and those compressed with potassium bromide, but these experiments have not yielded useable results as of yet (polycrystalline sulfur was not sufficiently IR transparent in our FT-IR spectrometer). Consequently, our intent is to pursue evanescent-based FT-IR analytical techniques using a contact attenuated total reflectance (ATR) cell. This approach provides the advantage of easier sample preparation and analysis. We are in the process of getting the details worked out on that method of characterization.

Figure 2.2. Left: Sulfur with polymerized carsul; Right: Distilled sulfur.

2.2 Chalcogenide Glass Manufacture and Characterization

Since ATR FT-IR analysis of polycrystalline sulfur is still under development, and since the ultimate objective is to fabricate pure chalcogenide glasses, it was decided to make an ampoule of arsenic trisulfide glass using purified sulfur and characterize its absorption spectra via FT-IR as means to evaluate the efficacy of the dynamic pyrolysis purification of sulfur. As mentioned earlier, we obtained ~ 23 g of purified (pyrolyzed and distilled) sulfur, which yielded an ampoule of As_2S_3 of ~ 55 g in total mass. Unfortunately, upon sealing the ampoule, the arsenic was overheated as seen in Figure 2.3.

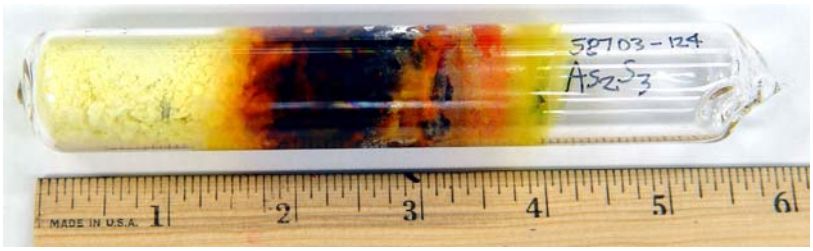

Figure 2.3. Photograph taken of the As_2S_3 ampoule after vacuum sealing with the oxy-propane torch. Some of the arsenic was overheated causing darkening.

The ampoule was rocked and annealed. A 1.39 mm thick window was cut and polished. Transmission FT-IR was performed on the window and the results are shown in Figure 2.4. The peak assignments of the absorbed impurities are labeled and summarized in Table 2.1. Even though these are only preliminary results obtained during this stage of the purification process development, a number of significant improvements can be noted in the FTIR spectra. First, the water (3600 – 3200 cm^{-1}) and the carbonyl (CO, 1600 cm^{-1}) absorption peaks were eliminated. Second, there was about a 65% reduction in the main H_2S absorption peak at 2500 cm^{-1} and the other H_2S peak at ~ 2300 cm^{-1} was essentially eliminated. Evidence that the dynamic pyrolysis had not been completed can be seen by the presence of the CS_2 peak at 1500 cm^{-1}. This is an indication that short-chained carsul had been formed in the sulfur during the preliminary pyrolysis step, and was carried over in the distillation process, and further polymerized during glass synthesis. This was anticipated, since pryolysis was not taken to completion. There was a new peak observed at ~ 2000 cm^{-1}, but it hasn't been identified yet. We suspect that it is also due to residual carsul present in the glass. We will verify this in the future experiments. The overall transmission of the As_2S_3 glass made with the purified sulfur was slightly less than specimens, previously processed in PNNL. This can be explained by the presence of black carsul deposits and bubbles that were observed in the specimen (not shown). The carsul deposits can be eliminated by completing the purification process and/or filtering the melt prior to solidification.

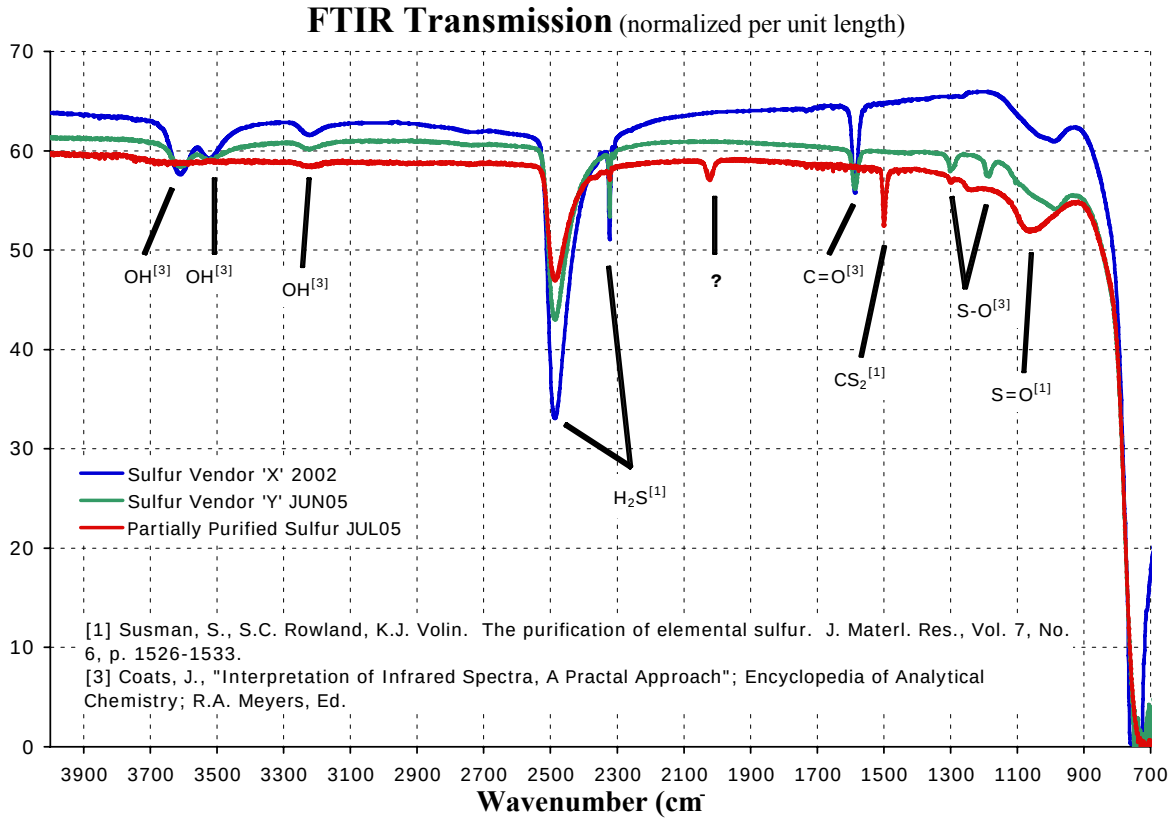

Figure 2.4. FT-IR spectra of various As_2S_3 glasses.

Table 2.1. Summary of common infrared sulfur impurity peak identities (Susman et al. 1992 and Coats 2000)

Mode	Species	Wave number (cm^{-1})	λ(μm)
OH str	OH	3620	2.76
OH str	OH	3540	2.83
-	OH	3220	3.11
SH str.	H_2S	2490	4.02
-	H_2Sx	2322	4.31
C=O str.	-	1589	6.29
CS str.	CS_2	1509	6.63
S-O	-	1300	7.69
S-O.	-	1190	8.40
S=O str.	Sulfoxide	1050	9.52

The noted reductions in absorption peaks demonstrate the progress made and the value of the dynamic pyrolysis purification of sulfur. It is important to point out that what was examined was not the final product, but only an initial analysis point to monitor the progress of the process, and determine its effectiveness. This particular batch of sulfur was only dynamically pyrolyzed for approximately 27 hr. Susman's paper reported a need to pyrolyze sulfur for up to 120 hr.

The window was also analyzed via optical microscopy. The specimen was found to contain bubbles as well as inclusions. The source of the inclusions was residual, soluble, partially pyrolyzed, C-S-H polymers formed during the early stages of pyrolysis that were carried over during distillation. (Note: There may have also been some particulate contamination during loading the chemicals into the ampoule.) Subsequent melting and reacting with arsenic during glass formation provided sufficient thermal energy to further polymerize the carsul, rendering it as insoluble, black inclusions in the glass. Complete pyrolysis of the sulfur to fully polymerize these contaminants will be required to eliminate them from the sulfur. The problem of carsul contamination in arsenic trisulfide can also be addressed by filtering the molten glass. The bubbles can be eliminated by longer processing times at higher temperatures.

Based on these characterization results, the following changes to the sulfur purification procedure will be implemented:

1. Dynamic pyrolysis will be done for longer times and at higher temperatures.
2. Distillation procedure will be improved to allow better heating on the receiver arm since the current setup results in the receiver arm clogging with condensed sulfur.
3. Glass processing will be done at higher temperatures and for longer times.
4. The molten As_2S_3 glass will be filtered to remove any residual carsul and particulate contamination formed during glass processing.

3.0 Chalcogenide Thin Film Glass Degradation Study

During routine testing and evaluation of As_2S_3 thin film based IR photonic devices and structures, a white surface haze was observed on some specimens stored under ambient conditions. This visible haze had a detrimental effect on component performance and appeared to be correlated to environmental conditions. Since field deployment of IR photonic devices will involve exposure to a wide range of environmental conditions, it is critical to understand the surface degradation process as well as develop strategies to prevent it.

3.1 Degradation Experimental Method and Results

To study this surface degradation, we evaluated the effects of visible light, oxygen, humidity, and temperature exposure on the films. An experimental matrix was developed to study the thin film's degradation process and to uncover any interdependency to environmental exposure conditions. Thin film samples were batched in an environmental exposure chamber and conditioned per the experimental matrix. White light emitting LEDs were used to expose the films. The study results showed that As_2S_3 films simultaneously exposed to light and water vapor formed arsenolite (As_2O_3) crystals on the film surface. This arsenolite formation is an oxidation process that corresponds to the surface haze observed in early As_2S_3 photonic devices shown in Figure 3.1. Without the combination of light and water vapor, the arsenolite did not form. Oxygen exposure did not produce any measurable effect while higher temperatures increased the oxidation rate. Details of this study were presented at the ACS, Glass & Optical Materials Division Fall 2004 Meeting (Allen, et al. 2004).

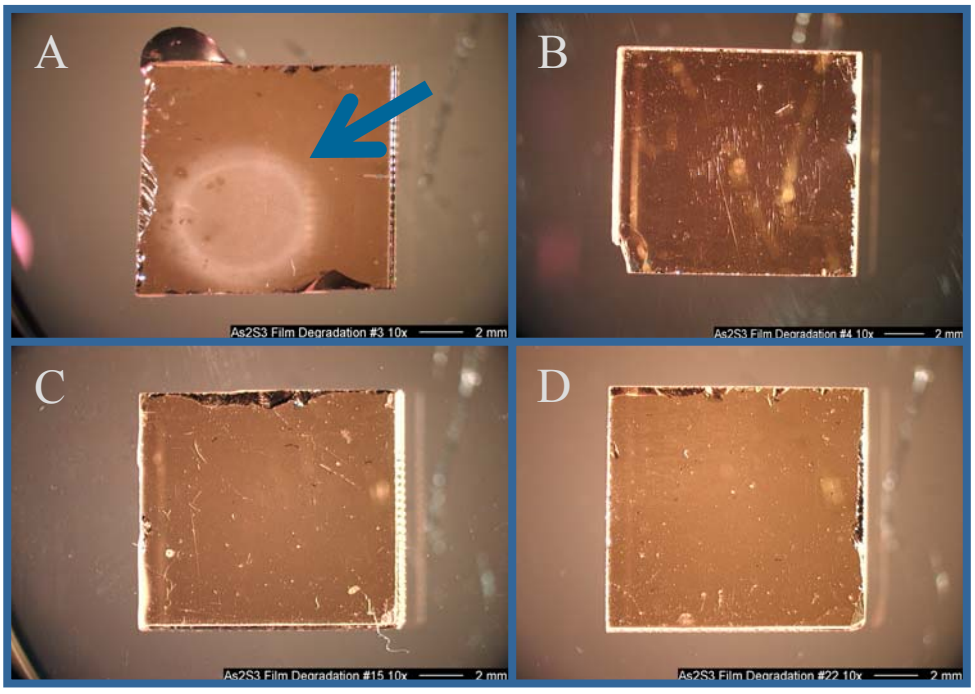

Figure 3.1. Visual image of samples exposed to (A) Light and Humidity (B) Light and Dry (C) Dark and Humidity (D) Dark and Dry. Circular pattern of degradation (A) corresponds to the cone of light from the LED.

3.2 Oxidation Wavelength Dependency

A second study was developed to ascertain the relationship between oxide formation and incident exposure wavelengths. As-deposited thin films were exposed to LED sources with wavelengths centered at 380, 405, 428, 470, 507, and 525 nm, with spectral emission properties shown in Figure 3.2. Samples were placed in an environmental chamber held at a temperature of 50 ± 1°C and relative humidity of 80 ± 5% for a duration of 14 days. (Note: in the following section samples are denoted by their LED exposure wavelength, e.g., sample 380 was exposed to the LED with a center wavelength of 380 nm).

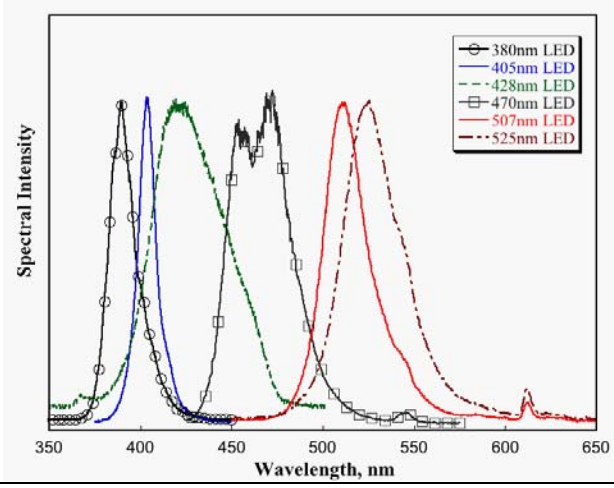

Figure 3.2. Spectral emission properties of the LEDs used in the second study.

Scanning electron microscopy (SEM), energy dispersive spectroscopy (EDS), and x-ray diffraction (XRD) were used to characterize the thin films before and after exposure. The results of the XRD measurements are shown in Figure 3.3. The spectra showed sharp peaks in samples 308 and 405 at diffraction angles 14°, 28°, and 35.5° corresponding to the spectra of arsenolite. Samples 428 to 525 did not have these peaks. The data also showed that only wavelengths below ~ 428 nm induced oxidation. Additionally, the XRD data showed the presence of a broad peak at ~16°, indicating the presence of realgar (As_4S_4). This peak was clearly present in the samples 308 and 405, reduced in samples 428 and 470, and considerably diminished for samples 507 and 525. The absence of realgar (As_4S_4) has often been used as an indication of completed thermal annealing of As_2S_3 and our previous research has showed that thermally annealed glass is very resistant to oxidation. This study indicates that exposing As_2S_3 to longer wavelengths has an effect similar to thermal annealing, thereby making it impervious to oxidation.

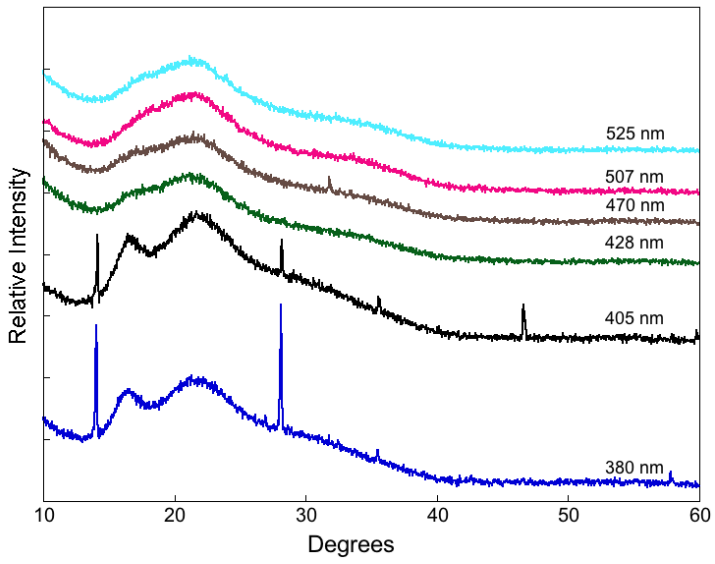

Figure 3.3. XRD spectra of as-deposited As2S3 thin films under LED light exposure at 50°C and 80% relative humidity for 14 days. The broad diffraction peak a ~22° is due to the substrate.

To corroborate the XRD results, SEM micrographs of all the sample surfaces were obtained. In Figure 3.4B, sample 380 clearly shows the presence of arsenolite crystals on the film surface confirming the XRD measurements. The SEM micrographs also showed the contrast between non-illuminated and direct illuminated regions for the sample 380, shown in Figure 3.4A and B respectively. The large structure in Figure 3.4B is an arsenolite crystal. Additionally, the film's surface exhibited a textured appearance. The illuminated region of sample 525, shown in Figure 3.4C, showed no response to the exposure conditions. SEM data collected for samples 428, 470, and 507 also did not show any observable arsenolite crystals.

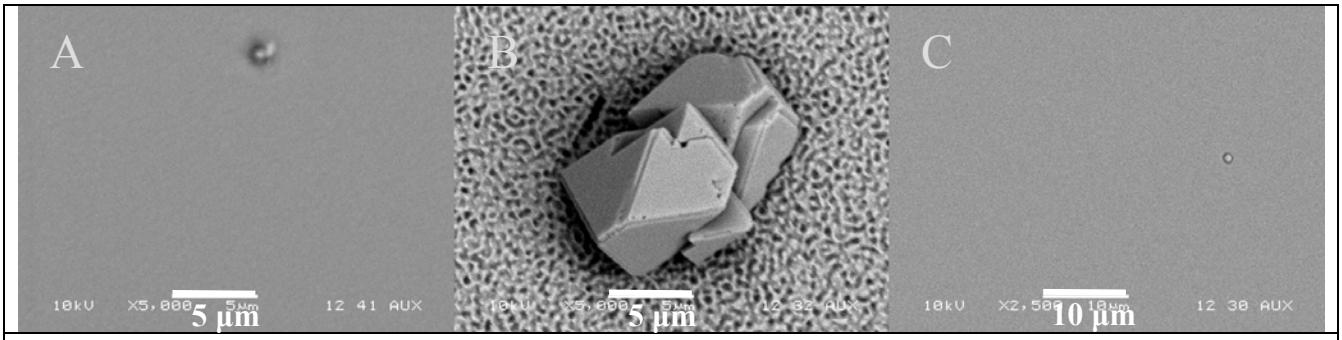

Figure 3.4. SEM micrographs of films subjected to fourteen days in the environmental chamber. (A) Sample 380, unexposed region (B) Sample 380, exposed region (C) sample 525, exposed region. The crystal in (B) is As2O3.

3.3 Degradation Study Conclusions

The results of this study showed that crystalline arsenolite formed on AS_2S_3 film surface only when exposed to both light (below 428 nm wavelength) and water vapor. Oxidation did not occur when the thin films were exposed to longer wavelengths, although XRD analysis clearly showed that a realgar reduction process, similar to thermal annealing, had occurred in these films.

We propose this wavelength-dependent oxidation of the film surface occurs for three reasons:

1. Mineral realgar is present to some degree in unannealed amorphous chalcogenide glass (Anheier et al. 2004). Conversion of realgar to arsenolite is thermodynamically favored when the chalcogenide films are exposed to water vapor and light. This reaction is photon energy dependant where we found that photon energies > 2.9 eV caused oxidation while photons with lesser energy did not. The reaction that drives realgar (As_4S_4) to arsenolite (As_2O_3) has a reaction threshold. Thus, exposing these films to shorter wavelength LEDs provide sufficient energy to drive the reaction while longer wavelengths will not drive this reaction even if exposed for a longer duration or with higher photon flux.

2. Photons below 428 nm are much more likely to be absorbed by the film. The penetration depth is less than 170 nm at 428 nm (Zallen 1983) and significantly less for shorter wavelengths. These photons are absorbed in only a fraction of the film volume adjacent to the film surface. The XRD and SEM measurements showed that arsenolite forms on the film surface only in the presence of a water molecule layer. Thus, the large photon absorption in a small area drives the reaction rate.

3. Wavelengths longer than 428 nm inhibit oxidation by reducing the amount of reactive realgar within the amorphous glass. We have shown that thermally annealed glass does not form arsenolite under the time scales and exposure conditions of this study. One method of determining the effect of thermal annealing is to measure As_4S_4 content via XRD. We found that the samples exposed to wavelengths longer than 480 nm had XRD spectra similar to thermally annealed samples. The reduction of As_4S_4, regardless of the cause - optical or through thermal annealing, does inhibit the arsenolite forming reaction from occurring. Thus, exposures to wavelengths longer than 480 nm inhibit oxidation.

Details of this study were presented at the 2nd International Workshop on Chalcogenide, Sinaia, Romania, June 21-26, 2005 (Allen et al. 2005a) and a paper was published (Allen et al. 2005b).

Practical results from this research include:

- Developed handling and storage protocols for thin films during processing and experimentation.
- Established integration and packaging requirements for photonic components made from these thin films.
- Long wavelength exposure could replace thermal annealing. The alternate glass stabilization method has shorter process time and reduces film delamination problem that occasionally occur during thermal annealing.
- Studies have shown degradation over extended periods of time is due to reversible processes in glass. This degradation can be prevented by developing a multipurpose coating that would reject wavelengths below 420 nm while at the same time be impervious to water vapor. In addition, the same coating could be designed to be an anti-reflection coating, a practical requirement due to the high refractive index of As_2S_3.

4.0 Chalcogenide Thin Film Deposition Research

Chalcogenide glass photonic components are normally fabricated in thin film structures. These glass films are prepared by thermal vacuum evaporation. Both single-layer (As_2S_3) and multi-layer ($As_2S_3 + As_2Se_3$) thin chalcogenide films were used to create laser-written waveguide and holographically recorded photonic structures.

A double planetary substrate holder, shown in Figure 4.1, was designed, fabricated, and installed in the chalcogenide thin film deposition system. Experimental measurements demonstrated significant improvements in the uniformity of film thickness, with variations less than 0.5% in a 2μm thick film across a 6-inch diameter sample holder. Improvements in the automation software continue to enhance vacuum deposition productivity. On average, two thin film depositions were completed each week of the fiscal year. These chalcogenide films were produced for a variety of projects that included film thickness monitor calibration, film uniformity experiments, optical index measurements (with prism coupler), shearing wave interferometer research, thermal annealing studies, and degradation experiments. A variety of film formats were developed and refined in support of the research, including: sharp steps, gradient steps, ribs, gradient ribs, and controlled large (>200%) to small (<0.5%) gradients over 3 to 6 inches.

Figure 4.1. A double planetary substrate holder developed to produce uniform film thickness.

5.0 Chalcogenide Glass Photomodification Research

In previous years, a laser writing station was developed and used to induce refractive index changes in chalcogenide glass (Anheier et al. 2004). A precision translation stage moves a sample with respect to a focused laser spot. A HeNe laser at $\lambda = 633$ nm is used, providing sub-bandgap exposure for As_2S_3 and bandgap exposure for As_2Se_3. A few changes were made to the setup shown in Figure 5.1, primarily to insure the polarization state of incident light on the sample, and also to provide more diversity for the wavelength of the writing beam. Polarization is known to influence the photodarkening effect, resulting in different refractive index changes for different input polarizations (Tanaka 2001). A polarization cube is used to insure a constant linear polarization during the writing of the patterns. A mirror on a flip mount is used to either send the beam from the HeNe laser or from an argon ion laser in the setup. This allows us to target different wavelengths that correspond to the various bandgap energies of the different chalcogenide glass. For instance, we can use the $\lambda = 514$ nm wavelength that corresponds to the bandgap energy of As_2S_3 and the HeNe beam at $\lambda = 633$ nm that correspond to the bandgap energy of As_2Se_3 to produce comparable effects in both glasses.

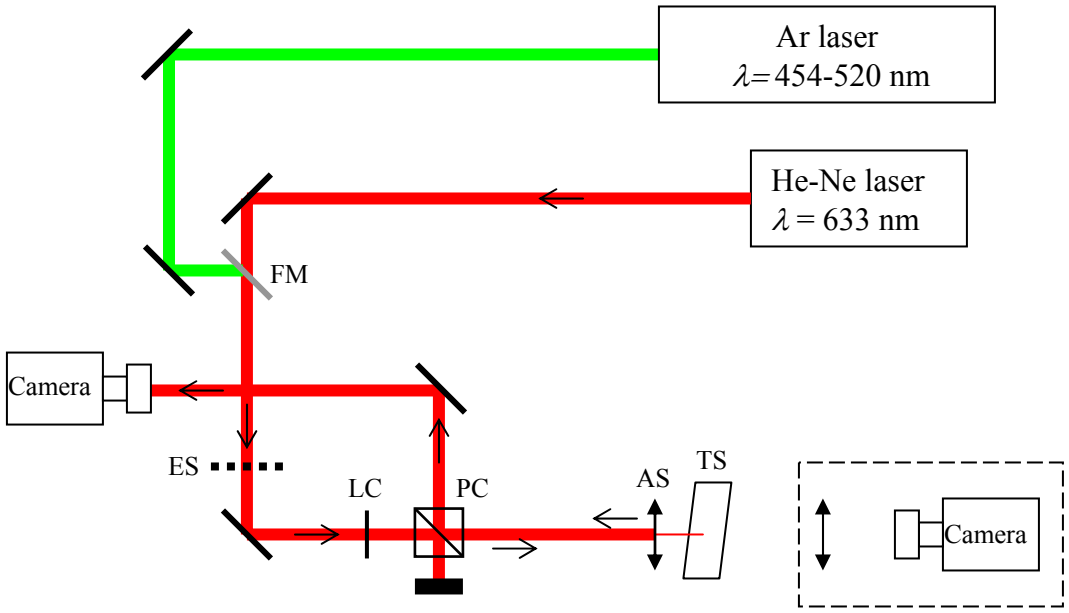

Figure 5.1. Laser writing station. A HeNe laser at $\lambda = 633$ nm and an argon ion laser are used. FM: Mirror on a flip mount that allows the beam from the argon ion laser to be sent in the laser writing setup instead of the HeNe beam. ES: computer controlled electronic shutter. LC: liquid crystal phase retarder used to control the writing power. PC: polarization cube that sets the polarization of the writing beam to linear. AS: three different aspheric lenses are mounted in a stage and can be used. TS: computer controlled three-dimensional translation stage holding the glass sample to be recorded in. The back reflected beam from the surface is imaged by the camera on the left to insure that the beam is well focused on the sample. The camera on the right is used the image the focal spot of the beam to determine its diameter.

Programs have been developed to write a variety of different patterns. Waveguides and arrays of waveguides were our main focus. In addition, the writing of waveguide couplers was also developed.

5.1 Effect of Annealing on Photodarkening

This project was done in collaboration with the University of Arizona as part of DOE's Faculty and Student Team (FaST) Program. For a duration of 10 weeks, two bachelor level students were included in our research team and had the opportunity of working on their own project, which we decided would be on the effect of annealing on photodarkening, a subject that is parallel to our own investigation of chalcogenide glass. Since the project was limited in time and involved students not trained in working in the field of optics and material science, the main focus was to introduce them to the field. Interesting results were nonetheless produced (Augustyn et al. 2005).

Several films of As_2S_3 were deposited in a single deposition run. Their thickness was 2.0 mm ± 1%. Transmission spectra were then obtained by using a spectrophotometer (Perkin Elmer Instruments Lambda 900 UV/VIS/NIR). Since the thin film on the substrate act as Fabry-Perot cavity, the transmission spectrum shows large oscillations. From theses oscillations, the thickness, losses and dispersion of the refractive index can be deduced by using the so-called Swanepoel's method (Swanepoel 1983). All samples showed similar transmission spectrum after they were removed from the vacuum chamber. These samples were then annealed at different temperatures. The ramp up and ramp down times were adjusted to keep the temperature variations constant at 1°C/min. Samples were annealed for 2 h at different soaking temperatures ranging from 120 °C to 170 °C. Transmission spectra were measured again and Swanepoel's analysis performed again to measure the difference in refractive index before and after the annealing.

The results are shown in Figure 5.2. As can be seen, annealing increases the refractive index of the films and the increase gets larger with annealing temperature. Saturation of the effect seems to occur for the last point, but more data would be required to confirm this.

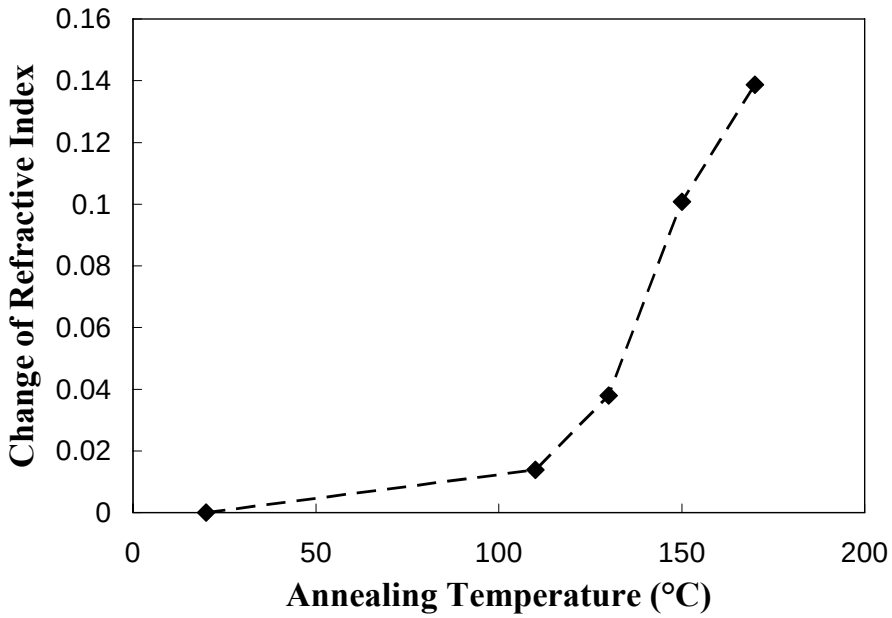

Figure 5.2. Annealing effects on refractive index.

No complete study of this effect has been reported yet, to our knowledge. There exists at least one study that compares the refractive index before and after annealing of thin films, but only for one annealing temperature (Laniel et al. 2003). This study is therefore very interesting from a design standpoint. However, the magnitude of the reported index change is 0.061 and it is doubtful such a large change can be induced. Even by photodarkening, which will induce larger changes, such changes would be considered enormous. Further study of the shortcomings of the method used for measuring the refractive index and of the experimental procedure was not done due to the

lack of available time from the students. In conclusion, the reported trend of the data is interesting, but the magnitude of the change should be investigated further.

6.0 Chalcogenide Glass Photonic Device Research

The chalcogenide glass photonic device research task focused on the design, fabrication and testing of novel integrated devices for the infrared. Specific attention was given to thin film devices, namely waveguides and couplers, this fiscal year. Devices were fabricated for use at $\lambda = 1.5$ μm, which allowed us to do preliminary work at a low cost. The issues of losses and injection efficiency were of specific importance, which lead to the development of multilayer thin films. A significant part of the work involved simulations to come up with the design of efficient LWIR devices. This work will form the basis of the development of more complex future devices.

Section 6.1 describes the design of near-infrared (NIR) thin film waveguides. The coupling station used to characterize the NIR waveguides is shown in section 6.2. Section 6.3 presents results on waveguide characterization. Results on multilayer thin film devices are shown in section 6.4, followed by results on waveguide couplers in section 6.5. Finally, section 6.6 addresses the design of LWIR waveguide devices.

6.1 Near Infrared Waveguide Research

Since the field of waveguide devices in the LWIR is largely unknown territory, the optical components and laser sources needed to characterize the devices are very expensive. In order to minimize our costs, part of the work was done in the near infrared a $\lambda = 1.5$ μm, since telecom laser diodes and low cost optical components such as microscope objectives, lenses, and mirrors, can be used. The experiments done in the near infrared were chosen so that their results can be extrapolated to the LWIR. This strategy allowed us to gain experience in working with thin film devices, to build a characterization bench, and explore issues that can be generalized to the LWIR at a low cost.

The design of the waveguide structure requires the consideration of many parameters. Since thin films are involved, the substrate needs to sustain the process of thin film deposition. The thin films must then be annealed. Finally, injection in the waveguide must be achieved by evanescent wave coupling, such as for grating coupling or prism coupling, or by end-fire coupling. End-fire coupling was chosen because it is simple and easy to set-up, even if it requires high quality input and output faces. Figure 6.1 shows the high quality faces are obtained by using a substrate that can be easily cleaved, such as silicon. Furthermore, wafers of silicon with a layer of thermal oxide are easily available at a low price. The thermal oxide will provide the guidance condition for the chalcogenide glass film. The refractive index of the chalcogenide glass ($2.4 < n_0 < 2.8$) will be greater than the refractive index of both the substrate ($n_0 = 1.45$) and the top cladding, which is air in the case of a single layer film ($n_0 = 1.0$). Wafers of a diameter of 76.2 mm were selected, which are large enough to accommodate the writing of long waveguides and make it easy to fit several at once in the vacuum disposition chamber.

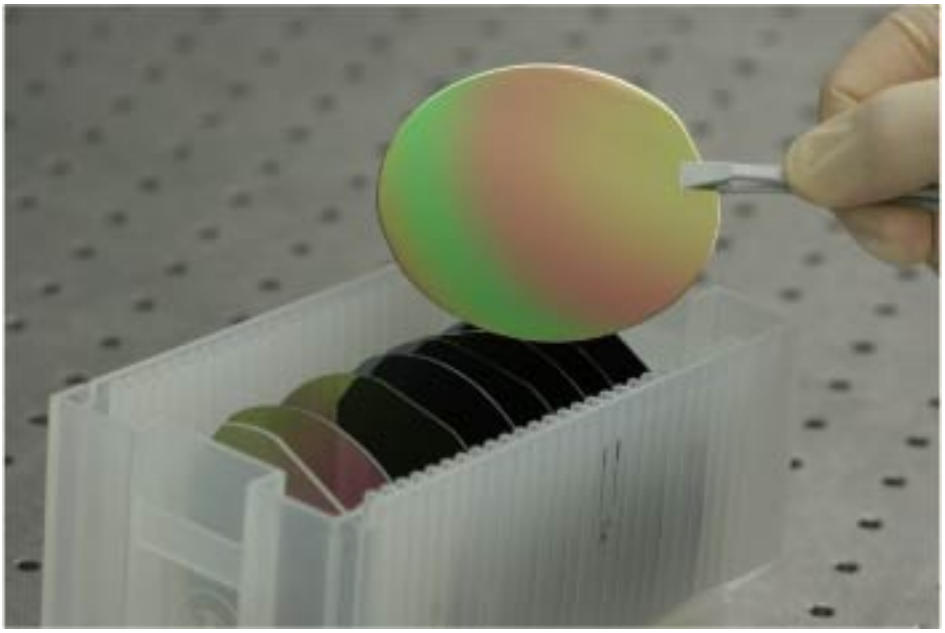

Figure 6.1. Silicon wafers coated with a thin film of As_2S_3.

The waveguide core was made of a thin film of As_2S_3 ($n_0 = 2.45$ at $\lambda = 1.5$ μm). The number of modes a film can support can be calculated from the solution of the guidance condition for TE modes in an asymmetric slab waveguide (Lee 1986). The results for the three first modes are shown in Figure 6.2. A monomode structure will then have to be thinner than 0.5 μm. The small size of the layer is due to the large refractive index difference between the core and the surrounding media. A reduction of this index difference leads to thicker monomode films structures, as will be shown in later sections.

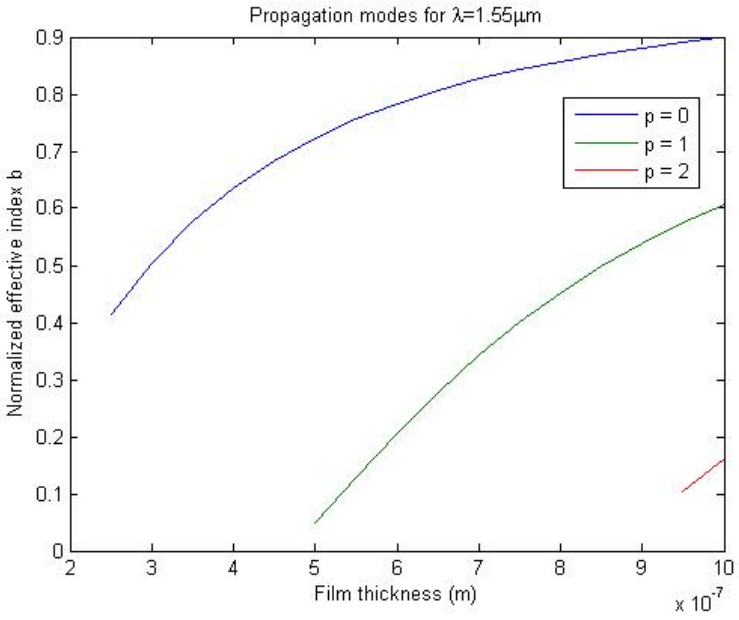

Figure 6.2. Propagation modes for different thicknesses of an As_2S_3 film. Below 0.5 μm, a single mode ($p = 0$) can propagate. The third mode appears close to 0.9 μm ($p = 2$).

Single mode structures were not attempted for single layer structures. The required thin film thickness would have made the injection process very inefficient since the input laser beam would always overfill the mode distribution. Instead, 1 and 2 μm thick films of As_2S_3 were used. The cleave quality is also paramount to the coupling efficiency. In order to achieve a proper cleave, the glassy film must adhere well enough to be substrate so that the silicon cleave will propagate through both layers of silica and thin film. Experiments showed that the efficient cleaving of the chalcogenide glass was indeed possible. The samples are cleaved with a diamond scribe, as usually done when working with semiconductor materials. Typical results are shown in Figure 6.3. When the substrate is only broken, the glass film does not have a high quality input face. To the contrary, when the substrate is properly cleaved, the glass film exhibits a very high input face quality. Both the input and output face must be cleaved.

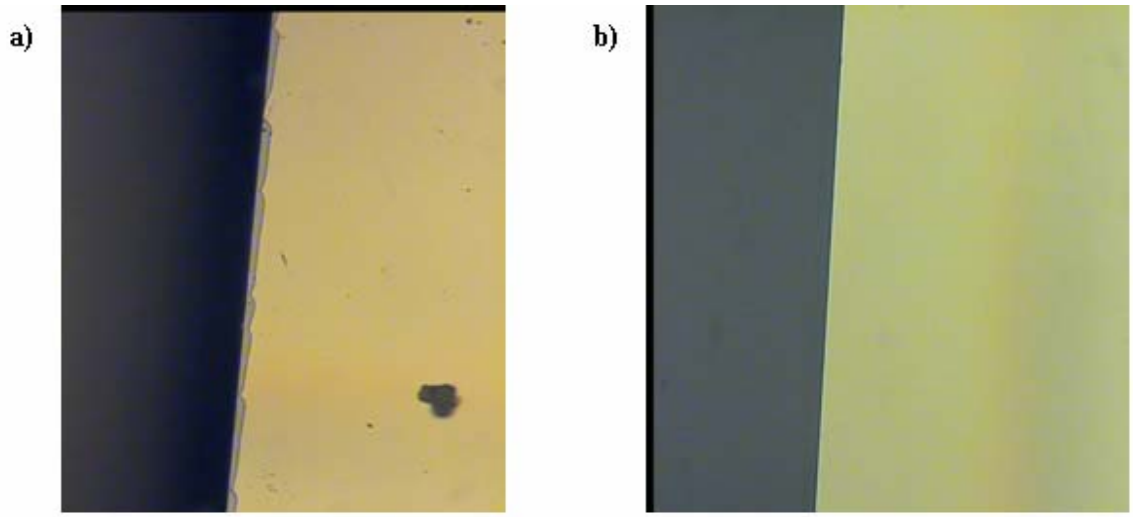

Figure 6.3. Substrate cleaving. The film, on the right of both pictures, is seen from the top at a magnification of 125x. a) The substrate is roughly scribed and the cleave did not propagate to the glass film, seen in a yellowish color on top of the gray substrate. b) The substrate is carefully cleaved with a diamond point. This time the cleave propagated through the glass film, resulting in a high quality input face.

The technique of laser writing was applied to create lines of higher refractive index that form optical waveguides. The thin film structure provides confinement in vertical dimension. The lateral confinement was provided by a local change in refractive index induced by the photodarkening effect, discussed previously in this report and in previous reports (Anheier et al. 2004). Typical waveguides will have a width of 4 μm and a maximum length of 4.5 cm, only limited by the size of the wafer and the travel of the translation stage used in the laser writing experimental setup. The increase in refractive index is usually of the order of $1x10^{-2}$. The number of modes such a structure can support can't be determined analytically and numerical tools must be used.

6.2 Waveguide Coupling Station

The waveguide coupling station shown in Figure 6.4 was use to characterize the fabricated waveguides. A telecom laser diode was used as the source. The TE polarization state at the input of the waveguide was achieved by using a polarization cube. Microscope objectives were used to couple light in and out of the waveguide and precision translation stages allow the alignment of the waveguide with respect to the focused beam. The output beam was imaged on an infrared camera.

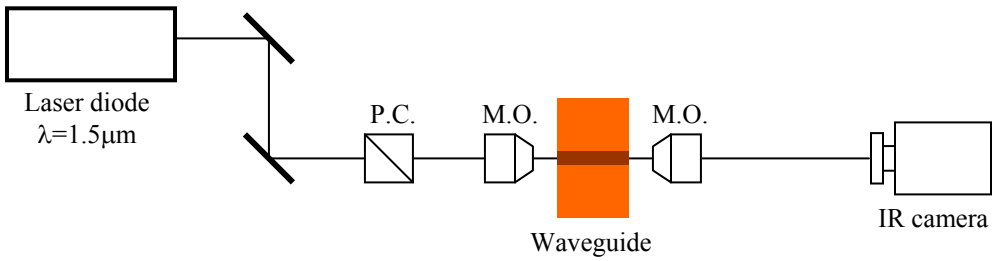

Figure 6.4. Waveguide coupling station. PC: polarizing cube, MO: microscope objective.

6.3 Waveguide Performance Characterization

The measurement of losses is of major importance to the development of integrated devices. Both thin film deposition technique and waveguide design can influence propagation losses. The losses incurred during light propagation have many different contributions. Intrinsic losses are due to the material itself and are the baseline for propagation losses. In addition, extrinsic losses also occur, created by scattering at the interfaces of different materials, for instance by absorption from impurities in the glass.

To measure the propagation losses, the waveguide coupling station was modified. Once the injection in the waveguide is achieved, a 2" mirror is used to redirect the light scattered from the film surface to the camera, now using an objective lens to form the image. A computer equipped with a frame grabber records the data. The nonlinearity of the intensity of the pixel is removed before the analysis and the pixel size is calibrated to provide a plot of the scattered intensity as a function of propagation length. The determination of the propagation losses is made by plotting the decay of the scattered light in the direction of propagation. Since the intensity of the scattering is proportional to the intensity in the waveguide, an exponential decay function can be fitted to the data to find the loss coefficient. The data near the input and output face was not included in the analysis since in these regions the signal is contaminated by the light either, not completely coupled into the waveguide or reflected from the end face. Analysis of a typical waveguide loss measurement is shown in Figure 6.5. A series of measurements on similar waveguides always resulted in loss values close to 1.5 dB/cm.

Our typical value for propagation losses in single layer is thus fairly large. Half the power is lost after every 2 cm. Since the refractive index between the core and the air is very large, $\Delta n = 1.45$, every surface imperfection has a large effect on losses. The roughness of the film thus induces large scattering effects, as can be seen from the data: the points in Figure 6.5 do not show a smooth exponential decrease and many spikes are seen. Another important parameter is the injection efficiency. However, this parameter was not optimized since the final device will operate at $\lambda = 8.5$ μm and will have a different design.

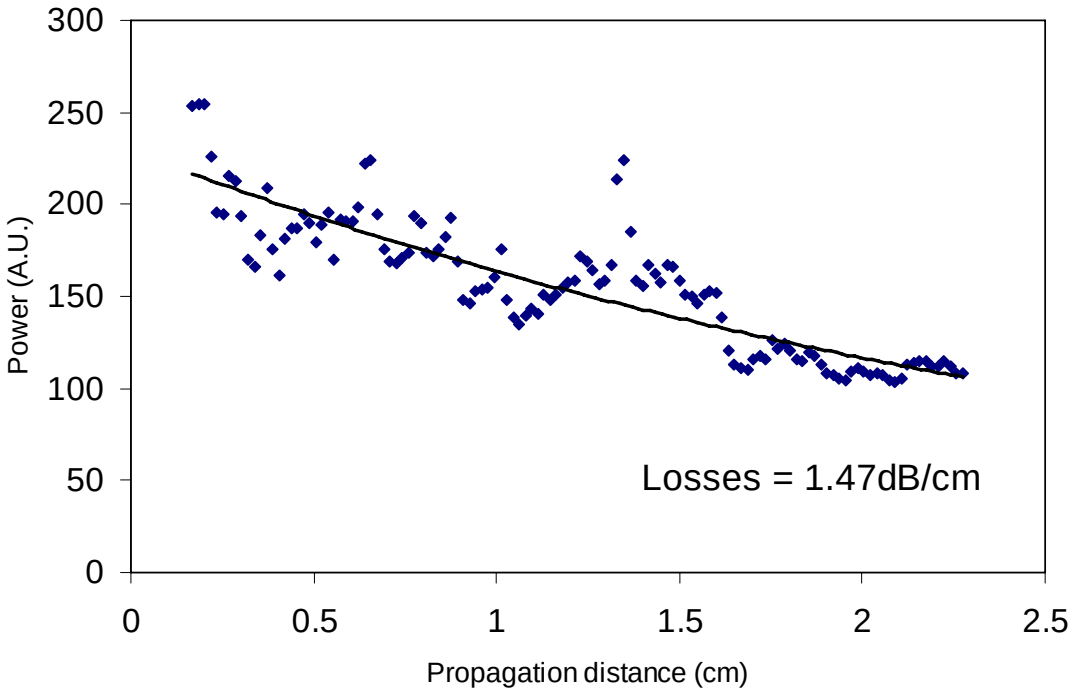

Figure 6.5. Propagation losses in single layer As_2S_3 film. An exponential decay function is fitted to the scattered light measured from the top of the channel waveguide. The points do not give a good fit to the function because of the large scattering from imperfections in the film surface.

6.4 Multilayer Waveguide Device

The measurement of losses was performed for multilayer devices to determine if the increased fabrication complexity leads to superior optical performance. Since the large refractive index change between a single layer film and the air superstrate leads to strong scattering, using a multilayer structure of SiO_2, As_2Se_3 and As_2S_3 should significantly reduce the propagation losses. The layout of this structure is shown in Figure 6.6.

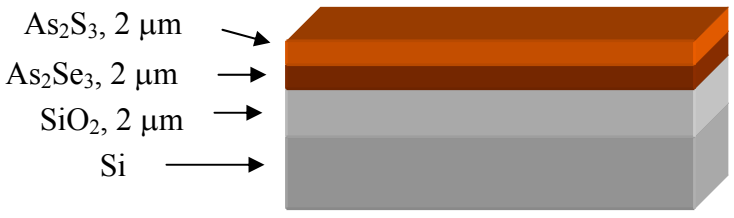

Figure 6.6. A multilayer chalcogenide thin film structure. The wafer is silicon (Si). The substrate is a 2 µm layer of silica (SiO_2, $n_0 = 1.45$), the core is a 2 µm layer of As_2Se_3 ($n_0 = 2.405$) and the superstrate is a 2 µm layer of As_2S_3 ($n_0 = 2.832$). The refractive index values are considered at $\lambda = 1.5$ µm and are taken from Laniel's paper.

The refractive index difference between the core and the superstrate is largely reduced when compared to the single layer case, down from $\Delta n = 1.405$ to $\Delta n = 0.427$. These two chalcogenide glasses were used because they are commercially available, but obviously the refractive index difference could be further reduced by using a better selection of chalcogenide glasses. Waveguides were recorded in the same manner as discussed in the previous section. Since As_2Se_3 is also photosensitive for $\lambda = 633$ nm, and even more than As_2S_3, the laser writing technique can still be applied. The waveguides were written with the same width as before for an easier comparison. Figure 6.7 shows the losses measured again using the scattered light from the top of the waveguides. The exponential decay fit revealed propagation losses of 0.48 dB/cm. Also, the experimental points did not show as much scattering centers as in the previous case, evidenced by the smoother distribution of the points.

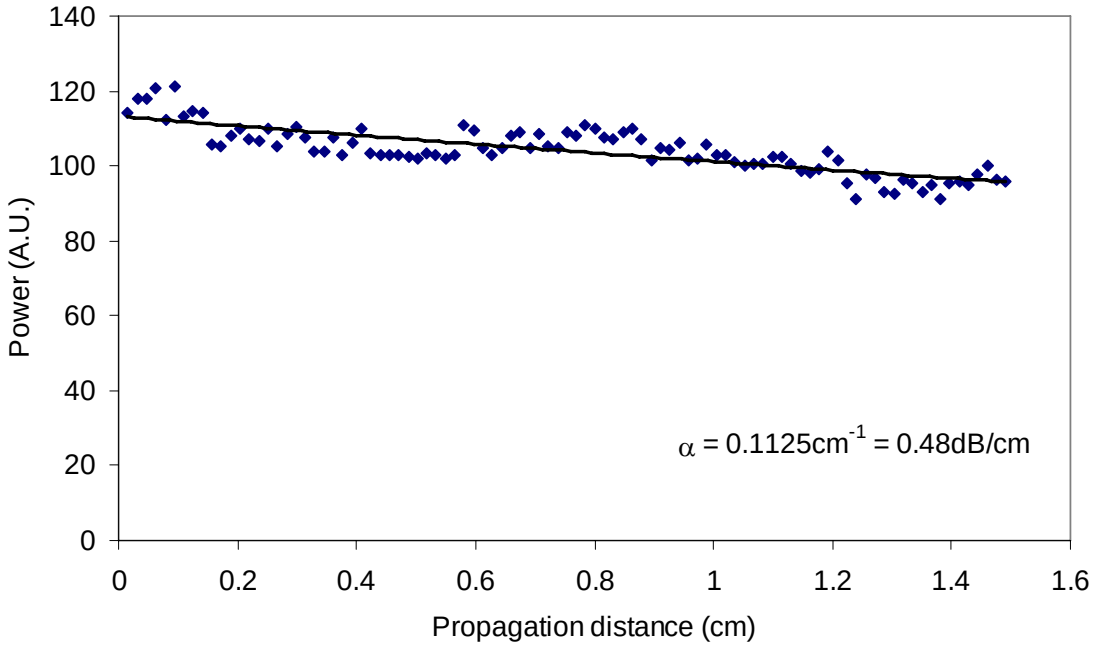

Figure 6.7. Propagation losses in multilayer chalcogenide glass thin film structure.

Figure 6.8 shows the original data obtained during the single layer and multilayer film loss analysis. The single layer presents many scattering centers, contrary to the multilayer slab. We can thus confirm that the use of a superstrate significantly reduces the propagation losses by 1 dB/cm.

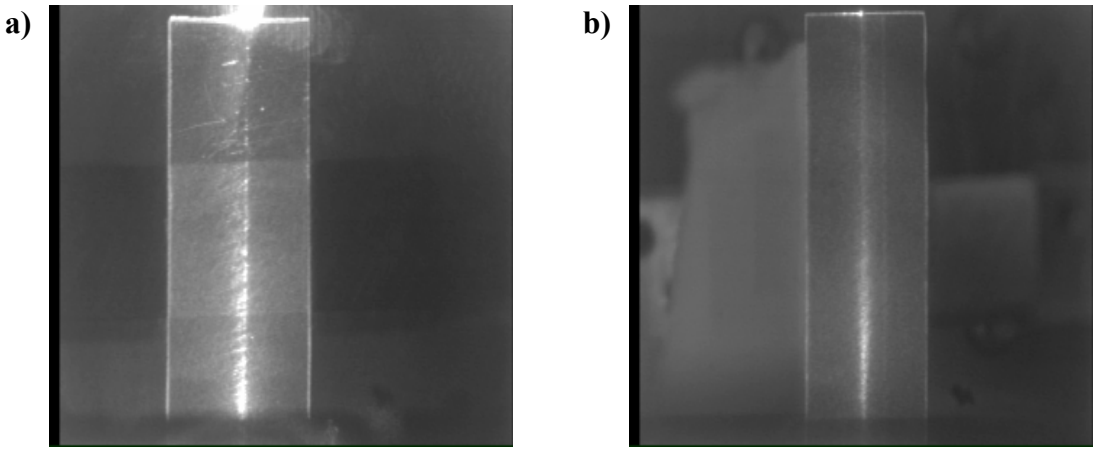

Figure 6.8. Waveguide light scattering comparison. a) Single layer film of As_2S_3. b) Multilayer films. The number of scattering centers observed from the top is clearly reduced.

The mode structure of the waveguides was also explored. By changing the input conditions, it is possible to see if higher order modes can be excited. In the case of the waveguides shown in Figure 6.9, two lateral modes could easily be excited. Vertical modes can't be resolved with the current imaging system, since the film is only 2 μm thick, which makes the attempt to image a vertical mode limited by diffraction. Using multilayer films also has the advantage of allowing larger single mode structure dimensions. The reduction in refractive index difference makes it possible to use thicker core films. As the core dimension increases, so does the injection efficiency. These conclusions will allow us to better plan the fabrication of efficient optical structures for the LWIR spectrum.

Figure 6.9. Lateral mode properties under different laser coupling conditions. Two lateral modes can be excited and are clearly seen.

6.5 Waveguide Couplers

The fabrication of optical waveguides is the first step in designing more complex optical devices. To demonstrate the feasibility of fabricating photonic devices in chalcogenide glass, the fabrication of a waveguide coupler was demonstrated. Waveguide couplers, or combiners, can be used for a variety of purposes. They might be used for monitoring the power of the laser by splitting a small portion of the beam and sending it to a detector. They can also split the input beam into many outputs to perform parallel experiments. Waveguide couplers are also the building blocks of more complicated systems. For example, the addition of two couplers can easily form a Mach-Zehnder cavity. Using couplers and gratings together makes temporal and spectral pulse shaping possible. All these reasons make the study of couplers worthwhile.

The waveguide coupler uses evanescent wave coupling to feed the propagating beam into the parallel waveguide. The two branches of the coupler are not in physical contact. When the two waveguides have evanescent fields that are mode-matched, coupling between the two waveguides can occur. Two waveguides of a width of 4 μm were recorded at a distance of 8 μm, center to center. The waveguides were straight, so coupling can occur over

the full length of the waveguides. The measured output profile shown in Figure 6.10, demonstrated that the power distribution was nearly 50% in each branch, as was typically seen for this length of the waveguides. Given the input laser has a narrow bandwidth, the distribution of power between the two branches will oscillates from one waveguide to the other as a function of length since they are similar and perfect mode matching is possible.

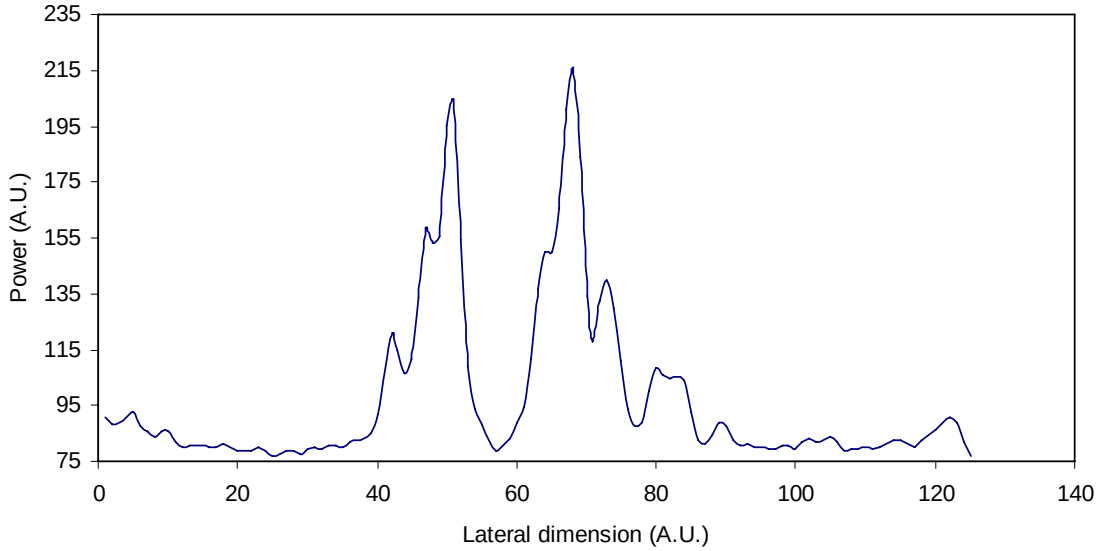

Figure 6.10. Power distribution at the output of an evanescent waveguide coupler.

6.6 Design of LWIR Optical Waveguide Devices

The previous results show the possibility of designing waveguide devices in chalcogenide glass and help foresee the issues involved in fabricating such devices for use in the LWIR. Multiple simulations and calculations were performed in order to design the structures needed to fabricate optical devices for the LWIR. This section presents an overview of the design that was done in order to prepare for the work of FY2006, when these devices will be used with QC lasers.

The waveguide structures for 8.5 μm propagation have significant design differences compared to the previous near infrared study. Above all, there is the issue of absorption. The materials that will interact with the propagating field must be highly transparent. In the structure presented in Figure 6.6, the core of the waveguide is in contact with a layer of silica, which is opaque in the LWIR. Using a different substrate could be the solution, but silicon wafers are cheap and can be easily cleaved, providing a simple way of injecting light into the waveguide. For substrates that are difficult to cleave, grating or prism coupling techniques must be used, making the design of waveguides more complicated since tapers will be required to mode-match the large input beam in the prism or grating to the small width of the channels. This is an involved process that would require a lot of design and fabrication time, so using a substrate that can be cleaved is advantageous. However, silica is opaque in the LWIR and silicon has a refractive index that is larger to that of chalcogenide glass, preventing the guidance condition. It will thus be necessary to first deposit a cladding layer of chalcogenide on the wafer, then a core layer of another chalcogenide glass having a larger refractive index, and then a superstrate layer, preferably of the same glass as the cladding layer. This will allow both the guidance condition and the high transparency. A glass such as As_2Se_3 is particularly well suited for the core layer. It has a large refractive index and its transparency window goes well beyond 10 μm. For the cladding and superstrate layer, most glasses in the As-S-Se family can provide the desired refractive index. However, a high proportion of sulfur limits transparency in the LWIR. For example As_2S_3 has a LWIR cutoff near 8 μm. Composite glasses are then the best option, such as $As_{24}S_{38}Se_{38}$ for instance.

Using two glasses that have a small refractive index difference is also an advantage since it will allow the fabrication of larger core size waveguides that can support a large mode. This is important to get high injection efficiencies, especially since the wavelengths in the LWIR are much longer than in the near IR, which makes them more difficult to focus down to a small spot size. The normalized effective index for several slab waveguide designs are shown in Figure 6.11. The materials considered for the substrate, the core and the cover are indicate in inset. The onset of the second mode, denoted $p = 1$, indicates where the waveguide stops being single mode. The graphs in Figure 6.11 a and b show the results for a multilayer structure of As_2S_3 and As_2Se_3, the largest refractive index difference used in this simulation. When other composite glasses are used, such as in Figure 6.11 c and d, it is possible to generate much thicker core layers. In graph Figure 6.11 d, the core can even be thicker than 11 μm. For such a thick core, the effective size of the mode will be large enough to allow efficient coupling. It should also be pointed out that these numbers are for an operation wavelength of 1.5 μm. For the LWIR, these numbers will be larger.

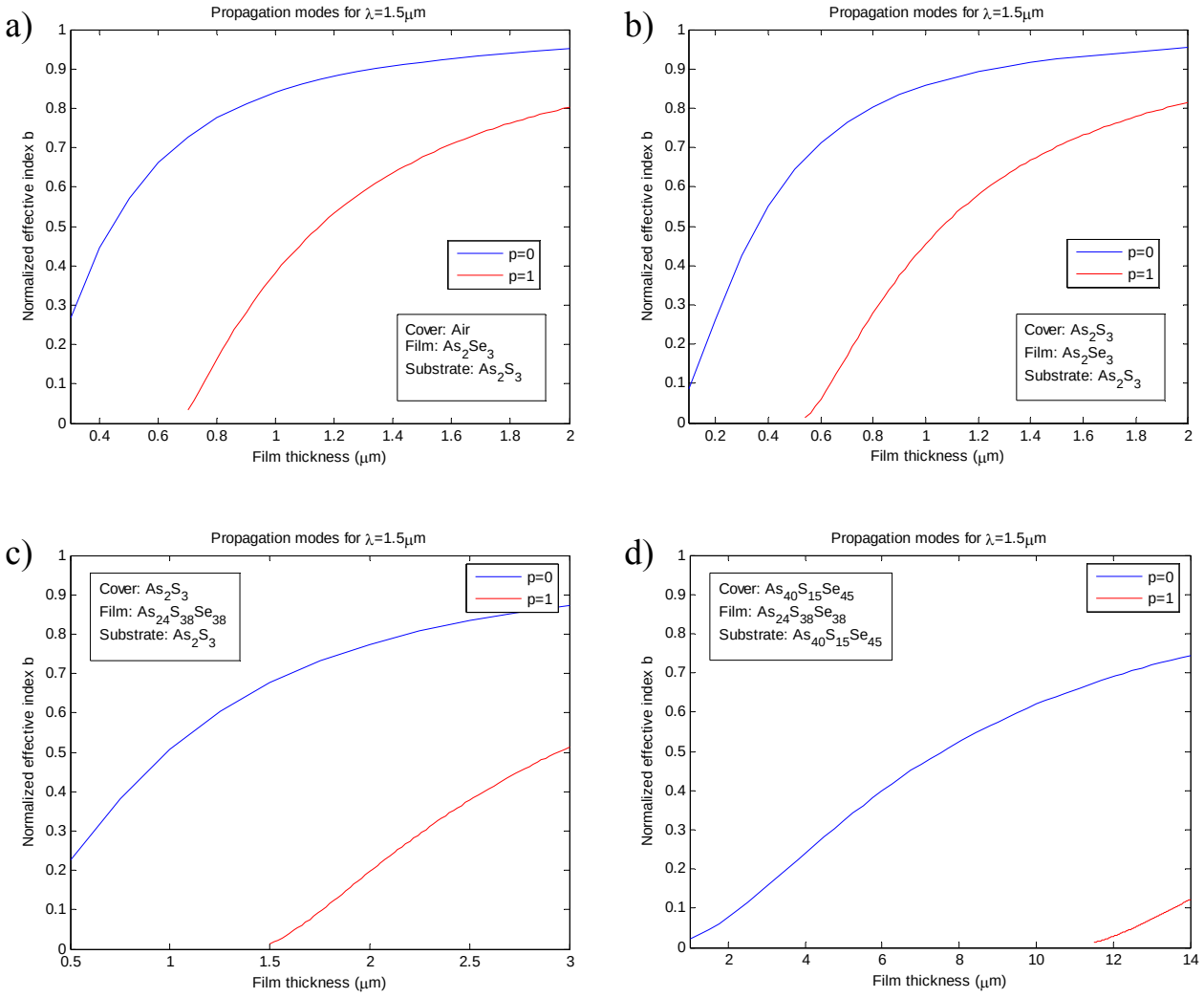

Figure 6.11 Normalized effective index as a function of core thickness for slabs of different combinations of glasses. The first mode is denote $p = 0$ and the second mode $p = 1$. The onset of the second mode indicates where the waveguide stops being single mode. The small Δn of the glasses used for slab *d* allows a very large single mode core.

The previous results involved calculating the normalized effective index of a slab, something that can be solved analytically. To the contrary, the effective index of a channel waveguide does not have an analytical solution and must be numerically determined. PNNL's Photonics Group made the acquisition of the well-known *BeamProp*™ software, from Rsoft Inc., which has the ability to simulate a large variety of waveguide devices. Waveguide couplers, for instance, can be numerically simulated. Specifically, this numerical tool will allow the precise design of several important photonic components. Two of these are presented here, a coupler used for laser monitoring and a multimode interference splitter with three outputs.

The designed coupler must pickup only 1% of the incident beam for monitoring the power of a laser. It is necessary to find the right distance at which to place the two waveguides and the interaction length over which the coupling will occur. After that length, one waveguide is bent so that both waveguides are at a large enough distance to prevent interaction of their supported modes. Figure 6.12 shows the results of such a simulation. The same simulation is computed for different distances between the waveguides and the output power of one arm is monitored, as shown in Figure 6.13. This numerical analysis provides a convenient method of coupler designing with any desired coupling ratio.

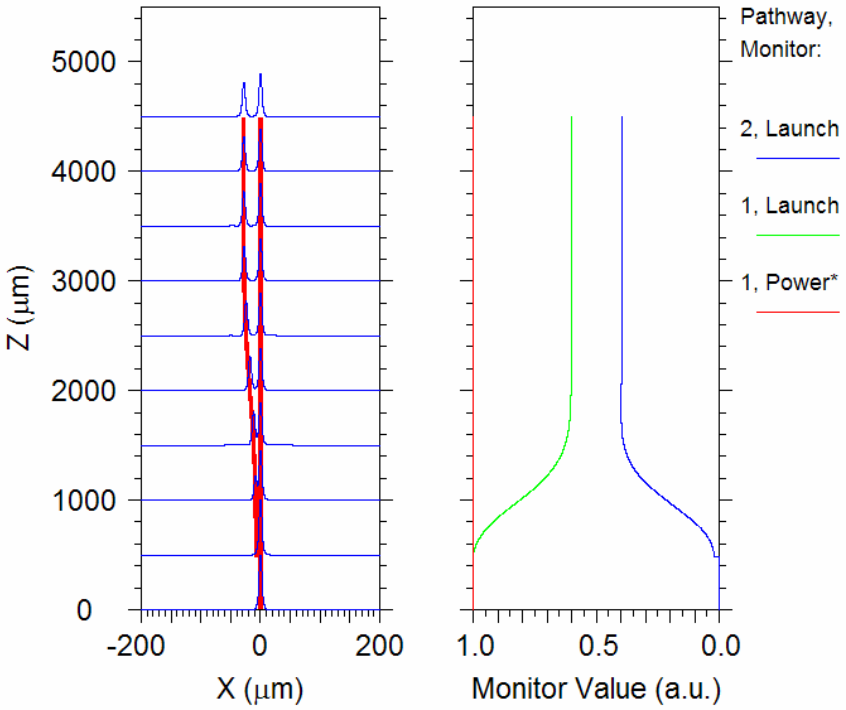

Figure 6.12. Numerical simulation of an evanescent wave coupler including a straight waveguide and a bent waveguide.

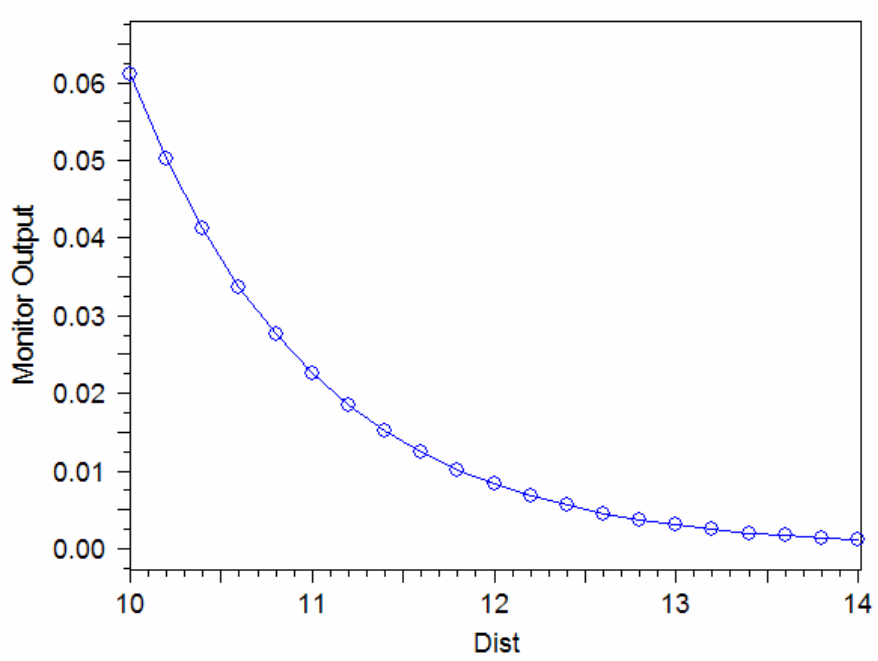

Figure 6.13. Coupled power ratio as a function of the center-to-center distance between two 4 μm wide waveguides.

A second interesting device is shown in Figure 6.14. Such a device is called a multimode interference splitter (or coupler). The input waveguide, at the bottom, sends the beam into the much larger waveguide. This wide region can support a multitude of modes that will beat together as they propagate. At particular propagation distance, nodes occur where the field is highly concentrated. This property makes it possible to place output channels that will capture the field and effectively create a splitter. This design has one input and three outputs, but a larger number of outputs are possible by decreasing the length of the interference region.

Overall, the structure of LWIR chalcogenide glass waveguides has been explored. The precise composition of the layers remains to be decided and will depend on the availability of the different compositions, either commercially or from PNNL's Non-Oxide Materials Synthesis Laboratory. However, the core material, As_2Se_3, is commercially available, so only the cladding material needs to be procured or fabricated. The presented results show the benefits of choosing glasses that will create small refractive index differences. Carefully choosing the glasses will allow the fabrication of large core waveguides that will have large injection efficiencies. Furthermore, we have developed the expertise to design complex photonic components by numerical methods.

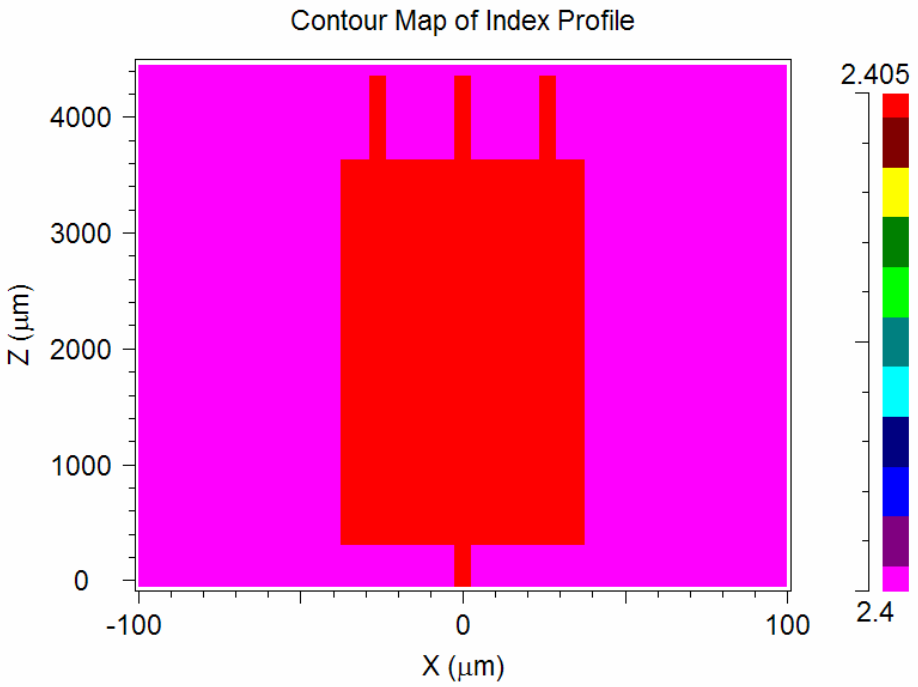

Figure 6.14. Refractive index change map for a multimode interference splitter.

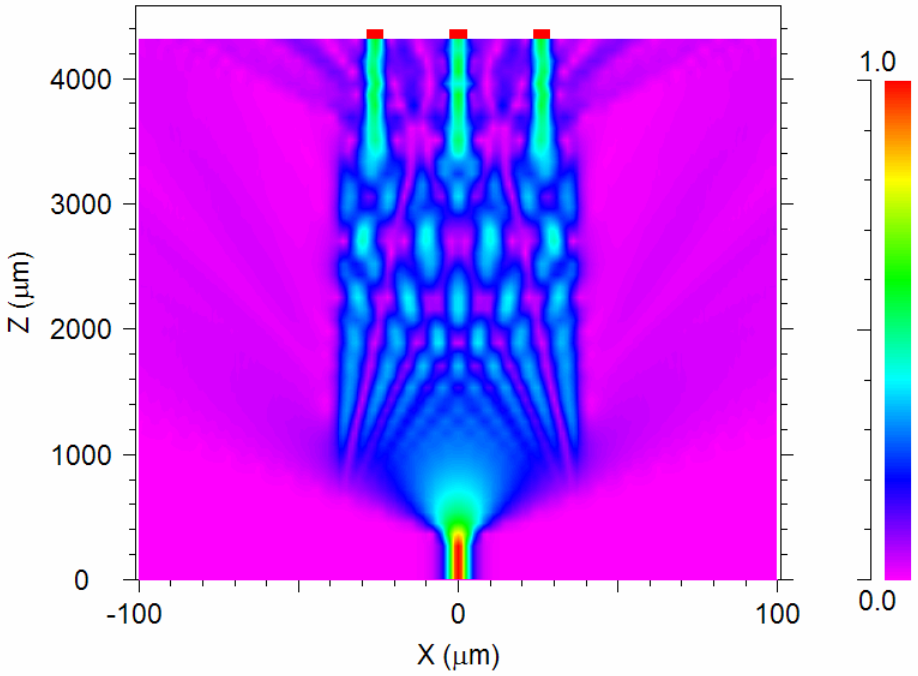

Figure 6.15. Intensity map in the multimode interference splitter. The power is divided in three equal parts at the output.

7.0 Advanced Optical Metrology

Photoinduced phenomenon in amorphous chalcogenide glasses have been extensively studied and reported (Kobolov and Tanaka 2001). The process of photomodification in As_2S_3 involves the absorption of incident photons by lone-pair electrons and their interaction with their neighbors. This often results in bond rearrangement such that normal As-S bonds have their length and angle modified, or even replaced by As-As and S-S bonds. This localized rearrangement of bonds increases the energy of the valence band, consequently decreasing the bandgap, resulting in photodarkening and altering its refractive index. Hence, exposure to laser illumination with photon energy either in or just below its band-gap results in increasing the refractive index in As_2S_3 (Anheier et al. 2004).

A major bottleneck in chalcogenide glass photomodification research is the ability to accurately measure the index change with high spatial resolution. The magnitude of change in refractive index is highly dependent on the characteristics of the illuminating laser beam (or writing beam) as well as the material properties of the thin film itself. In addition, the phenomenon of photoexpansion during laser writing has also been observed. Since the optical thickness of a photomodified region is the combination of both refractive index and thickness, the induced phase shift in that region is also due to the combination of both. Here, a shearing interferometer has been developed to accurately quantify the photoinduced phase shift resulting from this combination. This interferometer, when used in conjunction with a surface profiler, has the ability to provide an accurate measure of the photo-induced refractive index change in the material due to laser writing. Another important feature of this interferometer design is the ability to provide refractive index data with high spatial resolution. This is a feature that is especially useful for characterizing the gradient index structure created by laser writing, with its immediate application to waveguides. Section 7.1 provides a description of the shearing wave interferometer, along with a method of analyzing its interferograms, for characterizing photomodified chalcogenide glass.

The development of the QCL has provided a potential source of high-brightness, room temperature devices that provide high power laser output from 3 to 24 μm. The development of active and passive components needed to make useful devices at these wavelengths based upon chalcogenide waveguide structures requires specialized optics not readily available from catalog sources. Unfortunately, most of the commercially available optics at these wavelengths are specialized to either passive IR imaging or CO_2 beam delivery systems. Neither is suited to the task of collimating the highly divergent output from QCL devices nor mode matching collimated QCL or other sources for coupling into chalcogenide waveguides. Therefore, custom high to moderate numerical aperture aspheric optics must be procured and tested prior to use in our development activities. As all of these lenses will form real images, the ability to measure their transmitted wavefront in the long wavelength IR regime is really the only accurate way of assuring that their as-built performance meets the design specification. Measurement of aspheric surface figure using a commercial interferometer (at HeNe wavelength) would require either expensive computer generated holographic null elements (at approximately $5K per design) or optical surface profilers like the Taylor Hobson TalySurf (at approximately $200K). The LWIR Twyman-Green interferometer is an ideal and cost effective solution for our metrology needs. Section 7.2 provides a description of the Twyman-Green interferometer and the knife-edge scanning instruments.

7.1 Shearing Interferometer to Quantify Photomodification

Lateral shearing interferometry has been used in many diverse optical testing applications. One of its greatest advantages is its self-referencing configuration, making it easy to build and operate. Several texts are available, that describe this method in great detail (Mantravadi 1992). Also, several papers have been published describing unique applications of the shearing wave. For instance, the design of the interferometer described below was based on an apparatus designed to study the metal vapor and plasma created from an exploding wire (Pikuz et al. 2001). A brief description of the theory of a shearing interferometer is provided followed by a detailed description of the current apparatus and its analysis for measuring refractive index changes.

The method of lateral shearing interferometry is based on the lateral displacement of one wavefront by a small amount and then obtaining an interference pattern between the original and displaced wavefronts. Figure 7.1 shows the schematic of a lateral shear. If we consider the original wavefront to be a plane wave with small deviations, then the wavefront error may be described as $W(x,y)$, where x and y are co-ordinates of a particular point. Similarly, the sheared wavefront error can be expressed as $W'(x\text{-}S, y)$, where S is the amount of shear. The path difference (ΔW) between the two interfering beams provides is a measurable quantity, measured as an induced phase shift ($\Delta\Phi$), as the propagating wave traverses through the material. The measured phase shift in a propagating material can be expressed as

$$\Delta\phi = \frac{2\pi L}{\lambda}\Delta n$$

where Δn is the change in the refractive index, L is the thickness of the material, and λ is the wavelength of light in vacuum. Hence, if the thickness of a sample is known, it is possible to precisely calculate the refractive index by measuring the phase shift.

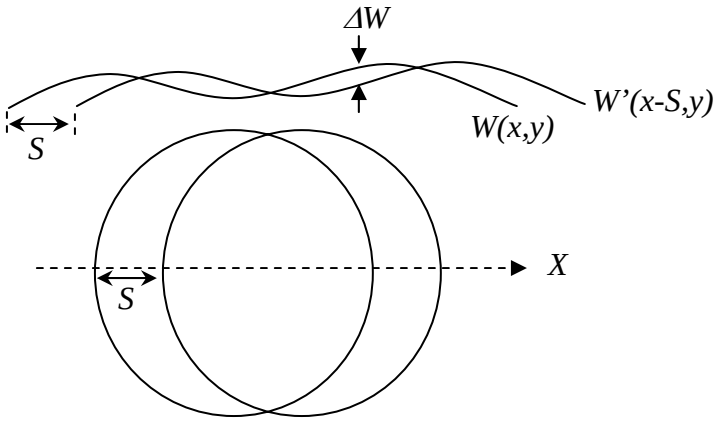

Figure 7.1. Schematic illustrating the interference of the original and laterally sheared wavefronts. The fringes are observed in the in the region where the two beams intersect.

This particular configuration of the lateral shearing interferometer was developed to measure changes in refractive index of chalcogenide glass, specifically As_2S_3, when laser written. The schematic of the shearing interferometer is shown in Figure 7.2. The apparatus is comprised of a frequency stabilized HeNe laser (Melles Griot 05-STP-901) that emits a beam of wavelength 632.8 nm with very high spatial and temporal coherence. The beam was spatially filtered and expanded to a size of ~25 mm in diameter providing a plane wavefront for the interferometer.

The sample was mounted on a stage that allowed translation along the X and Y axis, while also providing tip and tilt adjustment. To align the sample normal to the optical path, the iris diameter was reduced to roughly 1 mm and the sample tilted until the back reflection was coincident with the laser output aperture. The plane wavefront now travels through the photomodified As_2S_3 glass where a simple channel had been written, as shown in Figure 7.2, using the laser writing apparatus described in Section 5.0.

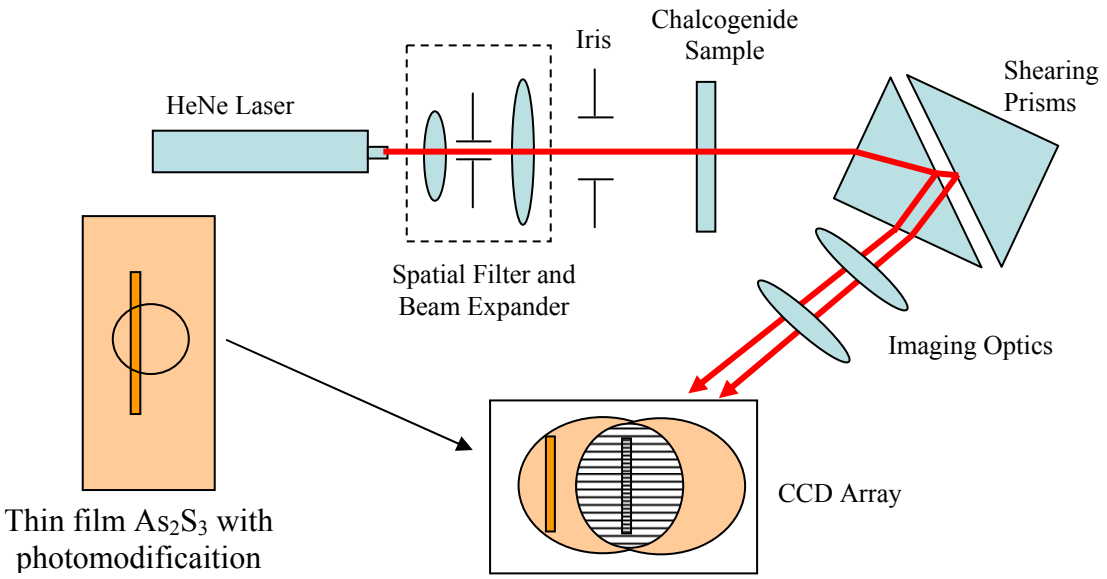

Figure 7.2. PNNL's lateral shearing interferometer built to measure refractive index changes in photomodified thin films of As_2S_3.

The shear prisms, which constitute the heart of this apparatus, were individually mounted on two extremely stable mounts (Newport 562 series) that provided X, Y, Z translation along with tip and tilt. Figure 7.3 shows a picture of the shear prisms mounted on these stages. This configuration made it possible to align the two shear surfaces of the prisms with high precision, providing full control of the shear and tilt required to obtain fringes that were parallel to either the x- or the y-axis. In addition, the precision of tilt provided full control over fringe spacing, such that the number of fringes available for analysis provides a good statistical sample. Currently, the prisms were tilted to provide ~15 fringes on the CCD array camera.

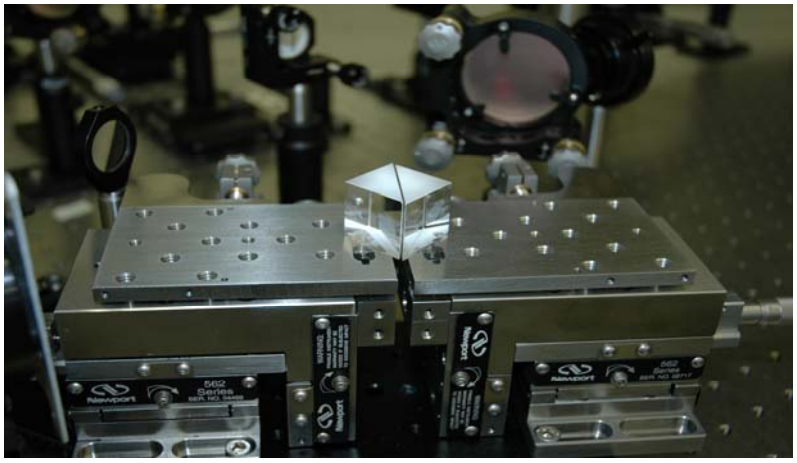

Figure 7.3. The shear prisms mounted on extremely stable Newport 562 Series stages provided the stability and precision required to fully control the fringe orientation, fringe spacing, and shear.

Since the photomodified region is extremely small with unmodified glass on both sides of it, as shown in Figure 7.2, it is essential to have a shear that is large enough to completely isolate the two complimentary images, with inverse phase shifts, such that they do not interfere with each other. The shear between the prisms for this experiment was ~2 to 3 mm, providing sufficient separation between the two images.

To obtain an image of a shearing interferogram, the wavefront at the surface of the sample needs to be imaged. A simple confocal imaging system was implemented with the sample placed at the focal length of the first lens and the CCD camera (Panasonic GP-MF-552), with its IR filter removed, placed at the focal length of the second lens. The CCD has a 640 x 480 array of pixels with a 5 μm x 5 μm pixel dimension. The interferograms were captured using a commercial frame grabber card. Figure 7.4 shows a typical interferogram obtained from a photomodified region of an As_2S_3 sample.

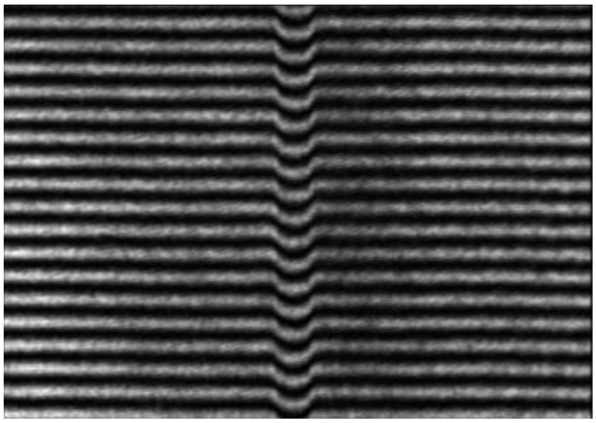

Figure 7.4. A typical shearing interferogram obtained from this apparatus showing a phase shift in the photomodified region of the sample.

A convenient way of analyzing non-contour type interferograms was reported where a Fourier transform on each column is used to determine the period of fringes (Takeda et al. 1982). Here, a shift in space corresponds to an added phase in Fourier space, from which it is possible to precisely calculate the fractional phase shift. Fringes are usually described by

$$g(x,y) = a(x,y) + b(x,y)\cos\left[2\pi f_0 x + \phi(x,y)\right],$$

which can be represented in a general way by

$$g(x,y) = a(x,y) + c(x,y)\exp(2\pi i f_0 x) + c^*(x,y)\exp(-2\pi i f_0 x)\,,$$

where $c(x,y) = \tfrac{1}{2} b(x,y)\exp(i\phi(x,y))$.

Since a Fourier transform describes an infinitely periodic function, using a truncated function, such as the interferogram bounded by CCD array dimensions, could lead to signal leakage into frequencies that did not exist in the real signal. Therefore, a Hanning window was multiplied by the original data set to reduce this effect. The Hanning window used here was defined as

$$w(x) = 1 - \cos\left[2\pi x / D\right]\,,$$

where D was the size of the window, which in this case was the size of the CCD array itself. The resultant interferogram, after applying the Hanning window, is shown in Figure 7.5 along with an intensity plot for a single column.

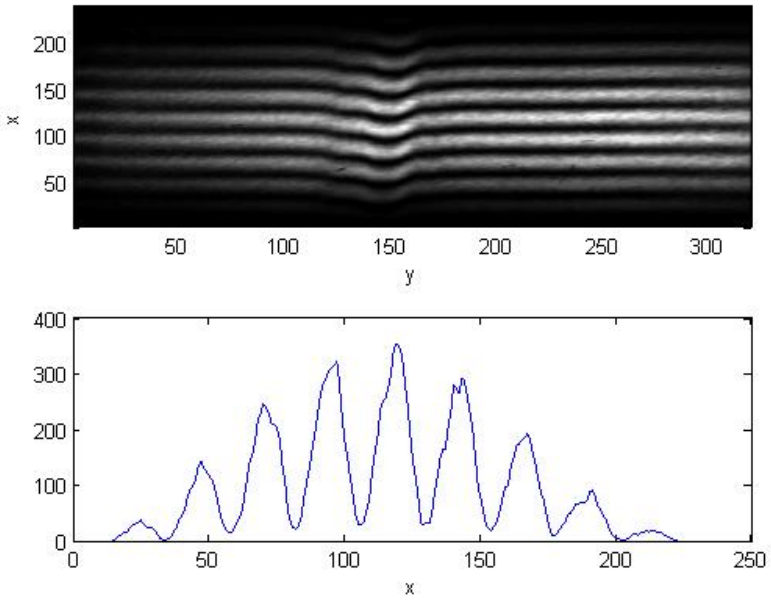

Figure 7.5. Resultant interferogram after applying a Hanning filter with a corresponding intensity plot along a single column.

Taking the Fourier transform of every column yields

$$\Im\{g(x,y)\} = \tilde{a}(f,y) + \tilde{c}(f - f_0, y) + \tilde{c}^*(f + f_0, y) \ ,$$

where f is the spatial frequency in the x dimension and f_0 is the carrier frequency. The power spectrum of the columns is shown in Figure 7.6.

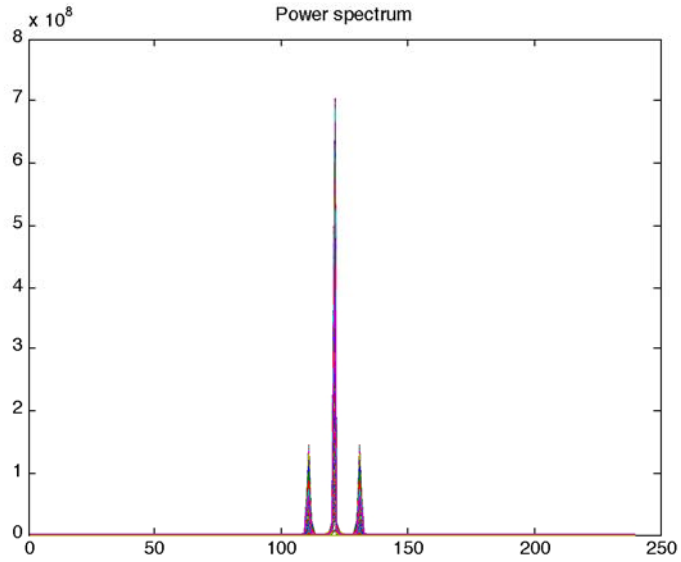

Figure 7.6. The power spectrum obtained after performing a Fourier transform on the data.

After obtaining the spectrum above, it is necessary to remove the central peak (i.e. the carrier frequency) and shift one of the other two peaks, either $\tilde{c}(f - f_0, y)$ or its complex conjugate, to the center of the window at f_0. Then, the other peak is also removed. Applying the inverse Fourier transform to the new spectrum $\tilde{c}(f, y)$ with respect to f, we obtain the $c(x,y)$, as defined above. The phase information for the above data is contained in the imaginary part of the natural logarithm of $c(x,y)$ expressed as

$$\mathrm{Im}\{\ln[c(x,y)]\} = \mathrm{Im}\left\{\ln\left[\tfrac{1}{2}b(x,y)\right] + i\phi(x,y)\right\} = \phi(x,y) \ .$$

This function, however, is bounded between $-\pi$ and $+\pi$ and discontinuities in phase need to be identified and corrected. The resultant phase change ($\Delta\phi$) across the entire cross-section of the interferogram along with a plot for a single column is shown in Figure 7.7. If the thickness of the film is known, then using the relationship between a change in phase and a change in refractive index

$$\Delta n = \frac{\lambda}{2\pi L}\Delta\phi$$

it is possible to compute the induced change in refractive index for every location along the writing beam. Figure 7.8 shows the photoinduced refractive index change in a thin As_2S_3 film. To illustrate the dependence of index change on the absorbed laser dose, the normalized beam profile of the writing laser is also plotted. The correlation between the laser beam profile and the photomodified region clearly shows that photomodification in As_2S_3 has a linear dependence on the absorbed laser dose.

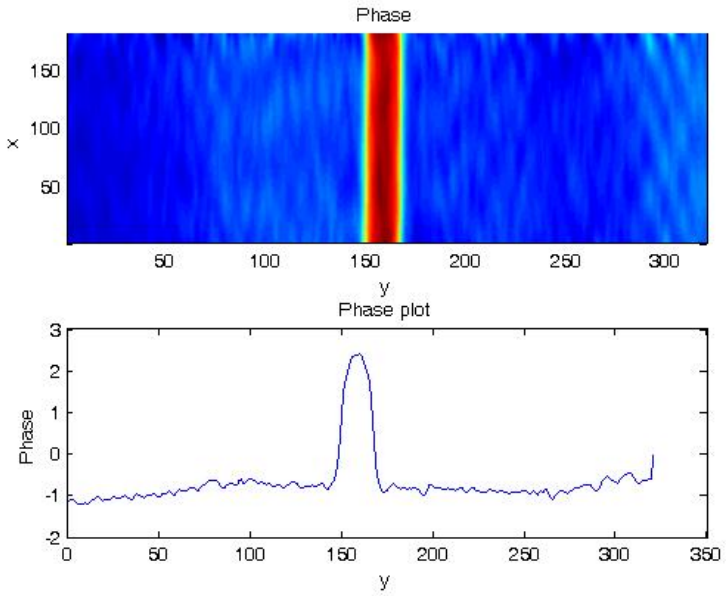

Figure 7.7. Phase change ($\Delta\phi$) measured across the cross-section of the photomodified As_2S_3 film along with a plot for single column.

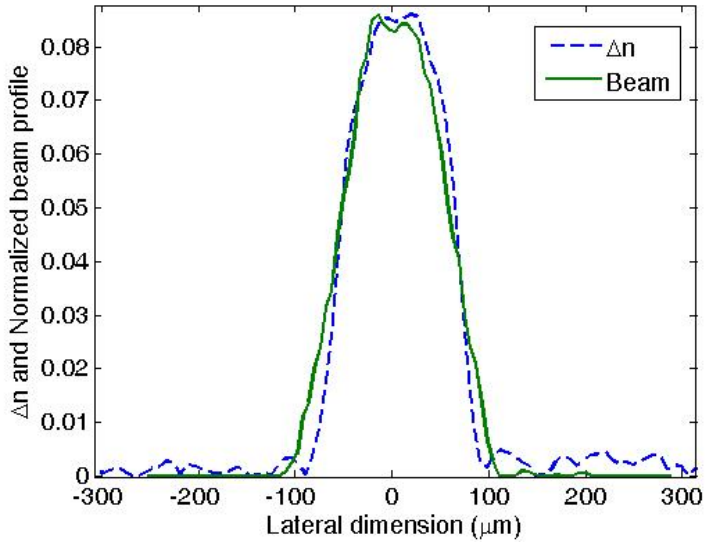

Figure 7.8. Resultant change in refractive index of a photomodified As_2S_3 film. The magnitude of index change is dependent on the laser dose absorbed, as evidenced by the overlap of the writing laser beam profile.

The measurements presented above were for an unannealed film of As_2S_3 with a thickness of ~3.66 μm deposited on a glass substrate. A 514 nm laser beam with a diameter of ~100 μm was used to write a channel in the As_2S_3 with a power of 15 mW and scan rate of 1 mm/min. After calibrating the image size to physical dimensions, it can be seen that there is good overlap between the index change in the photomodified region and the writing beam. The maximum index change observed in this sample was greater than 0.08, as shown in the Figure 7.8. However, it must also be noted that longer exposures resulted in a saturated top-hat profile for the refractive index change, indicating an upper limit for index change. Also, it is important to note that photomodification in As_2S_3 depends strongly on its material properties and its processing method. For instance, annealing As_2S_3 films significantly reduces the magnitude of available index change.

7.2 Long Wave Infrared Metrology Tools

Several chemical and biological sensing applications in the LWIR require specialized optical components that are not conventional off-the-shelf optics. Due to the unavailability of characterization tools in the LWIR, a suite of metrology tools have been developed to provide performance parameters at the wavelength of operation. This section describes a LWIR Twyman-Green interferometer to measure wavefront aberrations and a knife-edge scanner to determine the beam profile, spot-size, and M^2 values of an optic under test.

7.2.1 LWIR Twyman-Green Interferometer

The Twyman-Green configuration, originally developed in 1916, is simply a modification of the Michelson interferometer. The LWIR interferometer presented here uses a tunable CO_2 laser (LASY-4G, Access Laser Company) as its source equipped with closed loop water-cooling. It has emission lines in the range of 9.3 to 10.8 μm, with a beam diameter of 2.4 mm and a maximum power level of ~200 mW for a single line. The output of the laser passes through a half-wave plate (II-VI Inc., FRZ-8-12-.55-180-R) and polarizer (II-VI Inc., PAZ-15-AC-6),

which when used in conjunction with each other function as an attenuator without altering the polarization angle. The beam was then spatially filtered and expanded to produce a ~12.5 mm wide beam with a flat wavefront. Figure 7.9 shows a schematic of the LWIR interferometer. For this interferometer, the wavelength of the CO_2 laser was 9.4 μm.

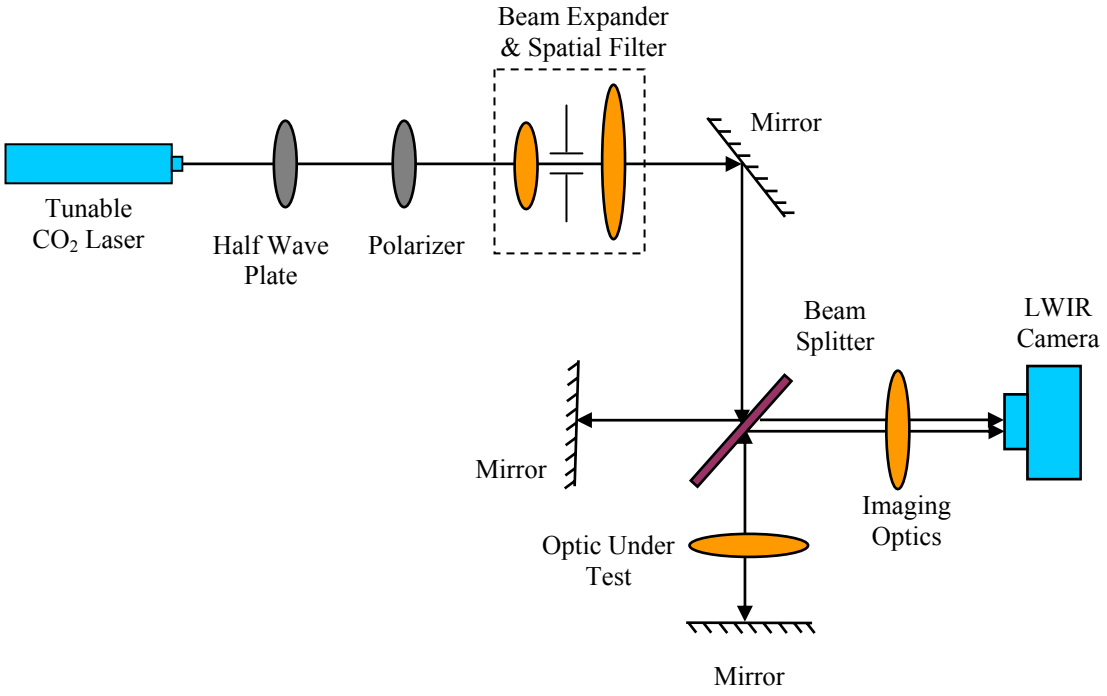

Figure 7.9. Schematic of a LWIR Twyman-Green interferometer to measure wavefront aberrations in custom made optical components.

The beam splitter (Janos Inc.) used in this interferferometer had a partially reflecting coating on the first surface and an anti-reflection coating on its second surface. In addition the beam splitter had a 2° wedge to minimize the fringing within the beam splitter. Here the wavefront is divided in amplitude and launched into the two arms of the interferometer. The reference path and signal path, with the optic under test in its path, are so aligned that they produce interference fringes on the camera. The camera (Electrophysics, PV-320) contained a 320 x 240 uncooled ferroelectric focal plane array with 50 μm x 50 μm pixel dimensions. The interferogram was first aligned to provide a null fringe after which a tilt was introduced in the reference path to obtain ~10 fringes on the sensor array.

In this experiment the optic under test was ZnSe *f/1* plano-convex lens with the back mirror located at its focal length such that the reflected beam retraced its path through the lens. Thus, the aberrated wavefront, due to a double pass through the optic under test, interfered with the reference beam to provide a characteristic fringe pattern on the sensor array. The imaging lens used for this apparatus had a long focal length of 150 mm arranged in a finite conjugate configuration with both the lens under test and camera at that distance. Figure 7.10 shows a typical interferogram for the lens under test obtained from this apparatus.

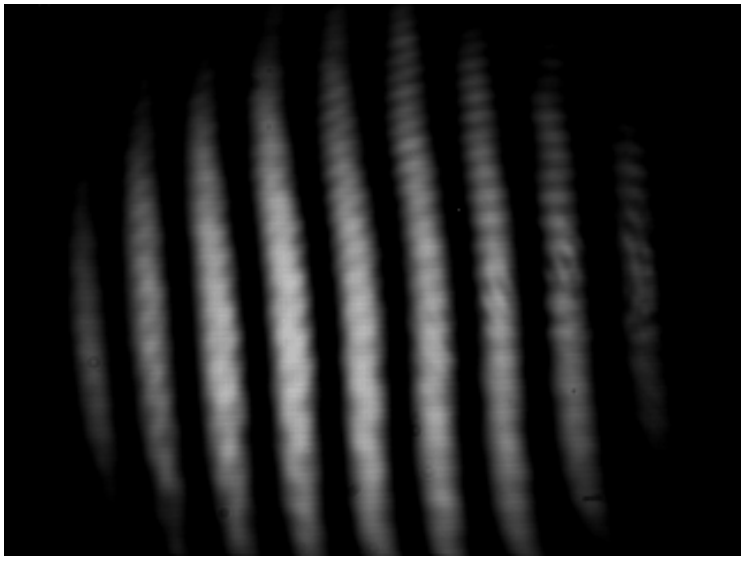

Figure 7.10. Interferogram of a ZnSe f/1 plano-convex lens obtained with the LWIR Twyman-Green interferometer

The optical path difference (OPD), or primary wavefront aberrations, in polar coordinates are expressed as

$$\boldsymbol{OPD} = \boldsymbol{A}\rho^4 + \boldsymbol{B}\rho^3\boldsymbol{Cos}\theta + \boldsymbol{C}\rho^3\left(1 + 2\boldsymbol{Cos}^2\theta\right) + \boldsymbol{D}\rho^3 + \boldsymbol{E}\rho\boldsymbol{Cos}\theta + \boldsymbol{F}\rho\boldsymbol{Sin}\theta + \boldsymbol{G}$$

where,

A = spherical aberration coefficient,
B = coma coefficient,
C = astigmatism coefficient,
D = defocusing coefficient,
E = tilt about x-axis,
F = tilt about y-axis, and
G = constant or piston term.

The above coefficients, also known as Seidel coefficients, represent aberrations in units of wavelength though most commercially available fringe analysis routines, such as Quick Fringe, allow for the removal of defocus (D) and tilt (E and F). A more precise method of describing the transmitted wavefront from an optic is to describe it by a set of polynomials, known as the Zernike polynomials (Malacara and DeVore 1992). Here, any arbitrary surface, or wavefront (*W*) can be described as a linear combination of circular polynomials expressed as

$$W(\rho,\theta) = \sum_{n=0}^{k}\sum_{l=-n}^{n} C_{nl} R_n^{|l|} e^{il\theta}$$

where $W(\rho,\theta)$ and $R_n^{|l|}$ are real, while C_{nl} maybe real or imaginary but must satisfy the condition $C_{n,l} = C^*_{n,-l}$.

Zernike coefficients describe the wavefront aberrations of an optic accurately up to the third order. These coefficients can be fed back into a ray tracing software (such as Zemax and Oslo) to better simulate the performance of an optic in an optical system. In addition, these polynomials can be used in the iterative design of custom lenses to minimize system aberrations and to subsequently verify optical performance. Figure 7.11 shows a schematic of the iterative design, fabricate, and test process for an optical component based on the data generated by this LWIR interferometer. The data shown in Figure 7.11 was from a commercially available ZnSe *f/1* plano-convex lens.

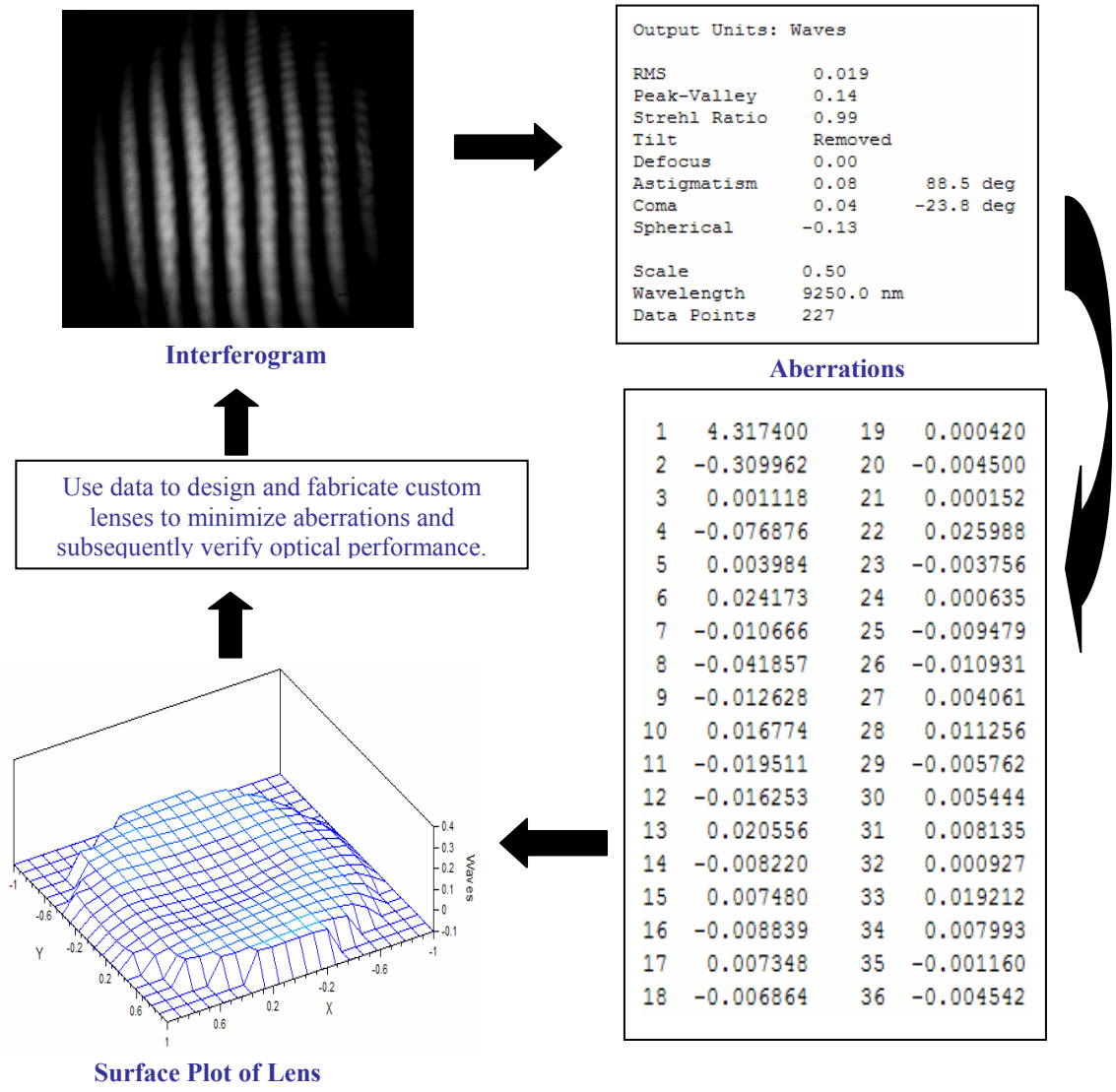

Figure 7.11. The iterative design, fabrication, and test cycle for minimizing aberrations in custom optics.

7.2.2 Beam Profiling with a Knife-Edge Measurement

In concert with the interferometric measurement for wavefront aberrations and its correction, it is also necessary to characterize the spot sizes obtained from the custom optics and to estimate its performance via a M^2 value (figure of merit), where the value of 1 implies diffraction-limited performance. In the past, LWIR cameras have been used measure spot sizes and beam profiles. However, the resolution of those measurements was limited by the 50 μm x 50 μm pixel dimensions of the focal plane array itself. This spatial resolution is not adequate for our needs; therefore a knife-edge scanning apparatus was developed. This apparatus incorporates a three-axis stage (New England Affiliated Technologies) with a precision of 2.5 μm per step to scan across the focal spot, thus providing superior resolution. The knife-edge scanning apparatus used the same CO_2 laser as the Twyman-Green interferometer, with the same attenuation and collimation optics described in the previous section. The CO_2 laser was modulated and the knife-edge signal detected using a MCZT detector in conjunction with a lock-in amplifier. Figure 7.12 shows a schematic of the knife-edge apparatus assembled to measure the spot size and M^2 values of the lens under test.

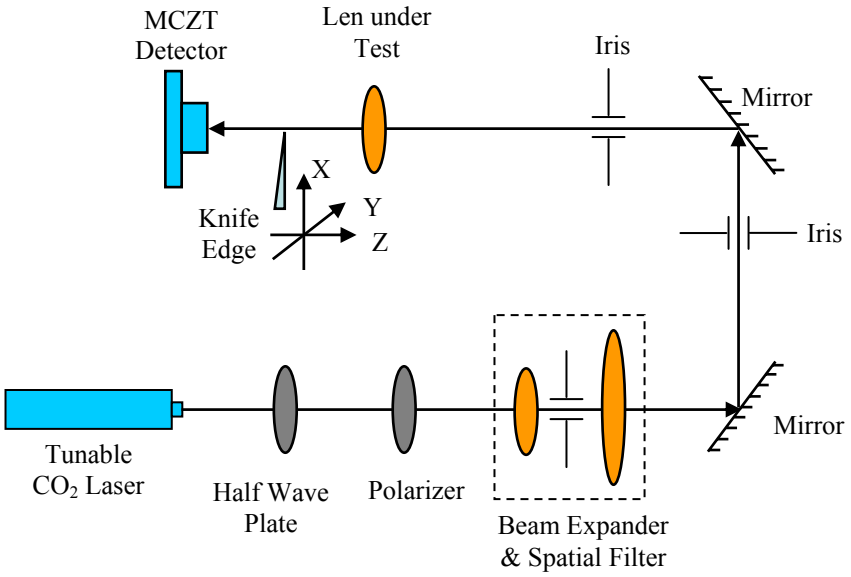

Figure 7.12. The Knife-edge scanning apparatus for measuring spot-sizes and M^2 values of the custom optics.

In this apparatus the optic under test, a ZnSe f/1 plano-convex lens, was mounted in a lens holder with five degrees of freedom (X,Y,Z,θ,ϕ) such that the lens would be absolutely normal to the collimated laser beam. The MCZT detector was placed at the focal length of the detector to initially optimize the alignment. The MCZT was then position behind the knife edge to collect the signal. The wavelength of the laser for these measurements was 9.4 μm.

Custom LabView software both controlled the knife-edge scan and collected the signal. Measurements were collected both sides of the focus. Knife-edge scans along the X-axis provided the intensity data, the derivative of which provided the shape of the beam at that location. A MatLab routine was written to automate the analysis of the acquired data. Figure 7.13 shows the experimental data, along with a Gaussian fit for a commercially available ZnSe *f/1* plano-convex lens under test.

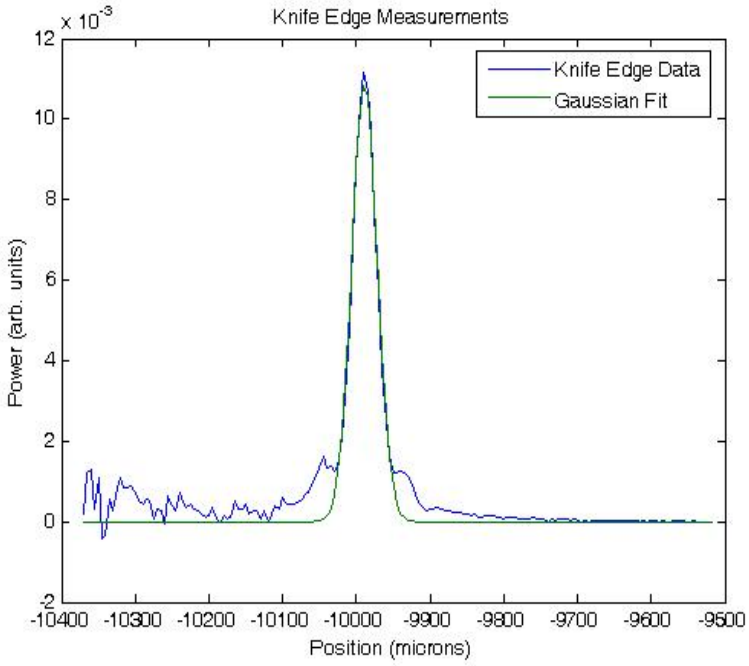

Figure 7.13. Knife-edge data for ZnSe f/1 plano-convex lens under test along with a Gaussian fit.

Using the Gaussian fit for each knife-edge measurement, the individual radii at every location was calculated. The figure of merit (M^2) for a propagating laser beam can be derived from the spot sizes measured along the optical axis. For this we used the expression for beam radius (ω) of a propagating Gaussian beam

$$\omega(z) = \omega_0 \sqrt{1 + \left(\frac{M^2 \lambda z}{\pi \omega_0^2} \right)^2}$$

where ω_0 is the radius of the beam, λ is the wavelength, z is the position along the optical axis, and M^2 figure of merit. Here, a M^2 value of 1 implies that the propagating laser beam has an ideal Gaussian shape. The measurement of M^2 at the focal plane of the test lens is a superposition of the test laser beam characteristics and lens under test aberrations. Since the beam characteristics of the gas laser are nearly ideal, any deviation from the ideal value of 1 can be ascribed to the lens under test. Figure 7.14 shows the results for the commercially available ZnSe lens under test. The M^2 fit for this lens yielded a value of 1 implying that this off-the-shelf component was a near-perfect lens.

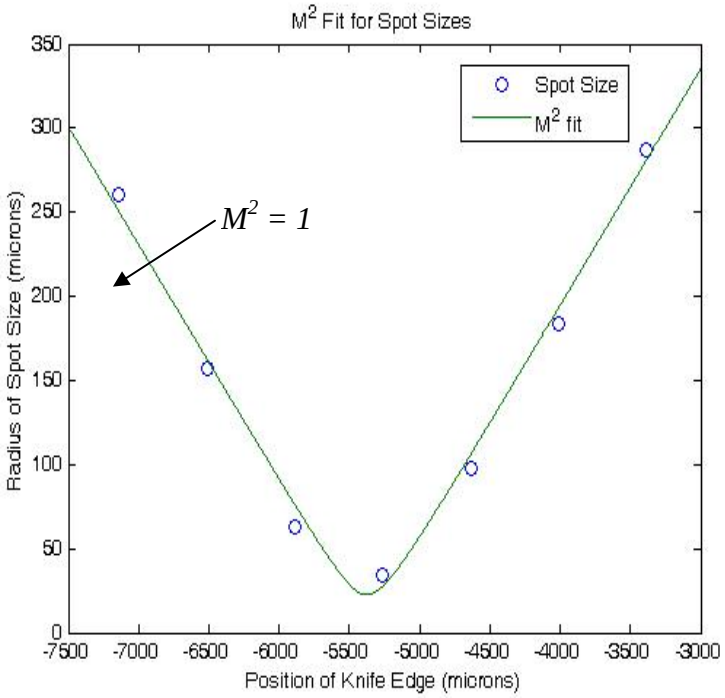

Figure 7.14. Radius of spot sizes as a function of distance for the ZnSe f/1 plano-convex lens along with a M^2 fit. The M^2 value of 1 implies that this lens was near perfect.

8.0 Summary

During FY 2005, PNNL's Infrared Photonics research team made measurable progress exploiting the extraordinary optical and material properties of chalcogenide glass to develop miniaturized integrated optics for mid-wave infrared (MWIR) and long-wave infrared (LWIR) sensing applications. We investigated sulfur purification methods that will eventually lead to routine production of optical quality chalcogenide glass. We also discovered a glass degradation phenomenon and our investigation uncovered the underlying surface chemistry mechanism and developed mitigation actions. Key research was performed to understand and control the photomodification properties. A shearing wave interferometer was developed for characterizing direct laser written channels in amorphous As_2S_3 glass with its immediate applications in the area of waveguide design and fabrication. A LWIR interferometer and knife-edge scanning station were developed to support the iterative design, fabrication, and test of custom optics needed for coupling QC laser light into the photonic devices.

The chalcogenide photonics research has laid the groundwork for the fabrication of LWIR photonic components. As a first step, optical devices were developed for the near infrared, where lasers and optical components are easily available. Also, single layer films can be used in the near infrared since silicon wafers can be oxidized, providing a low refractive index layer that allows a chalcogenide glass film to guide light. Thin films of 2 μm thickness were deposited on oxidized silicon wafers. Cleaving the wafers provided good input and output faces for the glass slabs. The laser writing station, developed in previous years under NA-22 funding, was used to record lines of increased refractive index having a width of 4 μm that can form optical waveguides. Output profiles and loss measurements have been reported. One the major result from that study is the beneficial effect of adding a cover layer on the waveguide's core. The losses were reduced from 1.5 dB/cm to a respectable 0.5 dB/cm when the cover layer was added. Waveguide couplers were also recorded and showed good coupling efficiency.

This work allowed us to consider the requirements needed to develop LWIR photonic devices. Our experiments and calculations allowed us to design a multilayer film structure that will support an efficient waveguide in the LWIR, allowing low propagation losses and high injection efficiency. Furthermore, several photonic devices have been simulated specifically considering chalcogenide glass.

9.0 References Cited in Text

Allen PJ, RT Baran, BE Johnson, MH Engelhard, BT Broocks, NC Anheier, JR, and SK Sundaram 2004. "Surface Degradation of As40S60 Thin Films." Glass & Optical Materials Division Fall Meeting, Cape Canaveral, Florida USA.

Allen PJ, BR Johnson, et al. 2005a. "Wavelength Dependence of Oxidation on As2S3 Thin Films." 2nd International Workshop on Amorphous and Nanostructured Chalcogenides, Sinaia, Romania.

Allen PJ, BR Johnson, et al. 2005b. "Photo-oxidation of thermally evaporated As2S3 thin films." *Journal of Optoelectronics and Advanced Materials* **7**(4): 1759-1764.

Anheier NC, PJ Allen, PE Keller, WD Bennett, PM Martin, BR Johnson, SK Sundaram, BJ Riley, JE Martinez, A Qiao, and JF Schultz 2004. *FY 2004 Infrared Photonics Final Report.* PNNL-15209, Pacific Northwest National Laboratory, Richland, WA.

Anheier NC, BR Johnson, and SK Sundaram 2004. "Laser writing in arsenic trisulphide glass," in *Optoelectronic Materials and Devices Vol.1,* eds. G Lucovsky and M Popescu, INOE Publishing House, Bucharest, Romania, pp. 259-295.

Augustyn V, XH Fan, P Lucas, BG Potter, KS Potter, SK Sundaram, BR Johnson, NC Anheier, JR, PJ Allen, N Ho, A Qiao, and BJ Riley 2005. "Cross-Correlation of Thermal and Optically Induced Structural Changes in Arsenic Trisulfide Thin Films." PNNL-SA-45971, Pacific Northwest National Laboratory, Richland, WA.

Coats J 2000. "Interpretation of Infrared Spectra - A Practical Approach" in *Encyclopedia of Analytical Chemistry."* R.A. Meyers, Ed., pp. 10815–10837, John Wiley & Sons Ltd, Chichester.

Kobolov AV and K Tanaka 2001. "Photoinduced phenomena in amorphous chalcogenides: from phenomenology to nanoscale" in Handbook of Advanced Electronic and Photonic Materials and Devices, ed. H.S. Nalwa, Academic Press, pp. 47-162.

Laniel JM, et al. 2003, "Refractive index measurements of planar chalcogenide thin films." *J. Non-Cryst. Solids*. **328**: p. 183-191.

Lee DL 1986. "Electromagnetic principles of integrated optics." John Wiley & Sons.

Malacara D and SL DeVore 1992. "Interferogram evaluation and wavefront fitting" in Optical Shop Testing, ed. D. Malacara, J. Wiley & Sons, pp. 455-500.

Mantravadi MV 1992. "Lateral shearing interferometers" in Optical Shop Testing, ed. D. Malacara, J. Wiley & Sons, pp. 123-172.

Pikuz SA, VM Romanova, NV Baryshnikov, M Hu, BR Kusse, DB Sinars, TA Shelkovenko, and DA Hammer 2001. "A simple air wedge shearing interferometer for studying exploding wires," Rev. Sci. Instrum., Vol. 72(1), 1098-1100.

Susman S, SC Rowland, KJ Volin 1992. "The Purification of Elemental Sulfur." *J. Material Res.,* Vol. 7, No. 6, pp. 1526-1533.

Swanepoel R 1983. "Determination of the thickness and optical constants of amorphous silicon." *Journal of Physics E*: Scientific Instruments **16**, pp. 1214-1222.

Takeda M, H Ina, and S Kobayashi 1982. "Fourier transform method of fringe pattern analysis for computer based topography and interferometry," *J. Opt. Soc. Am.*, Vol. 72(1), 156-160.

Tanaka K 2001. "Photoinduced anisotropy in chalcogenide glass, in Handbook of Advanced Electronic and Photonic Materials and Devices." H.S. Nalwa, Editor.

Zallen K 1983. "*The physics of amorphous solids*." John Wiley & Sons.

Distribution

No. of Copies

OFFSITE

LTC Ariel Cuadrado
United States DOE
NNSA/NA-22
1000 Independence Ave. SW
Washington, DC 20585

Dr. Rhys M. Williams
United States DOE
NNSA/NA-22
1000 Independence Ave. SW
Washington, DC 20585

Dr. David Berry
United States DOE
NNSA/NA-22
1000 Independence Ave. SW
Washington, DC 20585

Mr. Ralph Hastings
United States DOE
NNSA/NA-22
1000 Independence Ave. SW
Washington, DC 20585

Mr. Eric Sanders
United States DOE
NNSA/NA-22
1000 Independence Ave. SW
Washington, DC 20585

Mr. W. Randy Bell
United States DOE
NNSA/NA-22
1000 Independence Ave. SW
Washington, DC 20585

No. of Copies

Professor Henryk Temkin
Program Manager
DARPA/MTO
3701 N. Fairfax Dr.
Arlington, VA 22203-1714

ONSITE

32 **Pacific Northwest National Laboratory**

Allen, PJ	K5-25
Anheier, NC (4)	K5-25
Bruckner-Lea, C	K5-25
Clemmer, RG	K8-02
Dudder, GB	K8-29
Ho, N	K5-25
Krishnaswami, K	K5-25
Johnson, BR	K6-24
Riley, BJ	K6-24
Schultz, JF (10)	K5-25
Sharpe, SW	K8-88
Sundaram, SK	K6-24
Qiao A	K5-20
Information Release Office (7)	K1-06